DEVELOPMENT OF PIEZO-HYDRAULIC ACTUATION SYSTEMS TECHNOLOGY FOR USE ON A HELICOPTER TRAILING EDGE FLAP

A Thesis
Presented to
The Academic Faculty

By

Scott L. Herdic

In Partial Fulfillment
Of the Requirements for the Degree
Master of Science in Mechanical Engineering

Georgia Institute of Technology

December 2005

DEVELOPMENT OF PIEZO-HYDRAULIC ACTUATION SYSTEMS TECHNOLOGY FOR USE ON A HELICOPTER TRAILING EDGE FLAP

Approved by:

Dr. Christopher S. Lynch, Chairman
School of Mechanical Engineering
Georgia Institute of Technology

Dr. William P. King
School of Mechanical Engineering
Georgia Institute of Technology

Dr. David Sanborn
School of Mechanical Engineering
Georgia Institute of Technology

Date Approved: November 28, 2005

ACKNOWLEGEMENTS

I would like to thank my parents for their support of my endeavors, whatever they might be. I am grateful for the lessons and life they have shown me. They truly lead by example.

I would like to thank my graduate advisor, Dr. Christopher Lynch for his guidance in this research. I am grateful for the lessons in life and business gained through working with him.

I would like to thank my committee members, Dr. Sanborn and Dr. King for talking the time to read this thesis.

I would also like to thank my fellow graduate students for their assistance in the lab and willingness to listen.

Lastly, I would like to thank my wife for her devotion and support.

TABLE OF CONTENTS

LIST OF TABLES

LIST OF FIGURES

SUMMARY

The purpose of this study was to create a proof-of-concept piezoelectric actuator system capable of meeting the performance requirements necessary for actuation of a trailing edge flap for a helicopter main rotor blade. Due to extremely small displacements produced by piezoelectric actuators, their output is amplified several times in order to produce the required displacement for this device. The amplification is accomplished in two stages. The first stage, mechanical amplification, uses differential length lever arms to increase the piezoelectric actuator output. The second stage, hydraulic amplification, is coupled to the first stage and uses differential area pistons to further amplify the output of the mechanical amplifier. The actuation system's force and displacement output is characterized based on frequency.

CHAPTER 1: INTRODUCTION

This thesis discusses the development of a proof of concept piezoelectric actuator for use as the drive element in a blade-mounted trailing edge flap for a helicopter's main rotor. The primary focus of this research was to develop a suitable method for amplifying the small displacements produced by piezoelectric materials. Although the device developed in this research study does not fit the size requirements of a blade mounted actuator, the design is scalable.

The motivation for a trailing edge flap is to reduce vibrations induced into the helicopter airframe by main rotor aeroelastic effects. Prior research has shown that a blade-mounted trailing edge flap will substantially reduce vibrations. This will lead to a smoother ride for passengers and equipment, and also a substantial reduction in noise level. A future goal is to allow a similar device to perform primary flight control, minimizing the mechanical complexities present in current helicopter controls. An actuator suitable for flight control needs to develop substantially more output, compared with an actuator targeting vibration reduction.

Development of a piezoelectric trailing edge flap actuator has been the subject of ongoing research. The development of a suitable amplification technique has been the central focus of preceding investigations. Many amplification techniques have been employed. Early investigations utilized piezoelectric benders. The benders provided a convenient method of displacement amplification, but lacked the ability to provide sufficient force. Benders rely on an indirect piezoelectric effect that produces roughly a third of the output of direct actuation. As a result of these shortcomings, bender designs were abandoned in favor of designs using

piezoelectric stacks. Several displacement amplification techniques have been utilized. The most successful design, called the x-frame, was developed by a conglomeration of researchers including Boeing. This design was incorporated into a full-scale rotor blade and tested in a whirl tower. Although much progress has been made in this area, investigations still continue for an optimal solution that will provide a more efficient actuation method.

CHAPTER 2: PIEZOELECTRICITY

2.1 History of Piezoelectricity

The phenomenon of piezoelectricity was first discovered in 1880 by Pierre and Jacques Curie. Their experiments involving crystalline solids such as tourmaline, quartz, topaz, cane sugar and Rochelle salt exhibited surface charges when subject to mechanical stress (Piezo Systems 2002). This behavior was named "piezoelectricity." This behavior of materials developing electric charge due to a mechanical stress was further clarified as the direct piezoelectric effect. The discovery that these materials would also produce a mechanical strain proportional to an applied electric field, known as the converse piezoelectric effect, brought about this clarification. The combination of these two effects is now known as piezoelectricity.

Following the discovery of piezoelectricity, work was done within the European scientific community and it was determined this behavior was due the lack of center symmetry in the crystal microstructure. Further investigation revealed that 20 out of the 32 crystal classes lack center symmetry and therefore can develop piezoelectric effects (Jaffe, Cook et al. 1971). Thermodynamics was used to further clarify the complex relationships between mechanical, electrical, and thermal variables.

The first device to use piezoelectricity was an ultrasonic submarine detector, which was developed during World War I. The device utilized quartz sandwiched between two steel plates. The device was excited underwater by an electrical signal (converse piezoelectric effect), and it would emit an ultrasonic acoustic signal. The signal would travel through the water and reflect off of any objects it contacted, such as a submarine. When the reflected signal returned to the

detector, it would mechanically excite the detector and develop an electrical signal as a result (direct piezoelectric effect). The time that occurred between the signal's departure and arrival to the detector could be used to determine the distance to the reflecting object (Piezo Systems 2002). This development was the beginning of sonar, which is still a modern subject of research.

Following World War I, other piezoelectric devices such as microphones, accelerometers, transducers, bender actuators, and phonograph pick-ups were invented. These devices had limited performance due to the materials available at the time (Piezo Systems 2002).

In the early 1940s, several different researchers in different parts of the world observed that barium-oxide/titanium-oxide compositions had an extremely high dielectric constant of around 1100. The highest dielectric constant that had been previously observed was that of rutile (TiO_2) which was around 100 (Jaffe, Cook et al. 1971). It was later determined that the high dielectric constant was due to ferroelectricity, of which piezoelectricity is a subclass. These ferroelectric materials exhibited a substantial increase in piezoelectric properties compared with naturally occurring piezoelectric materials.

In 1954, it was discovered that lead zirconate titanate $Pb(Zr,Ti)O_3$ exhibited superior piezoelectric properties compared with existing materials (Trainer 2003). Both zirconium and titanium atoms have a +4 oxidation state, so they are substitutes in the unit cell. By modifying the percentages of zirconium and titanium, manufacturers are able to tailor material compositions to achieve desired properties for a given application, such as stiffness, dielectric constant, and piezoelectric coupling. This enabled the creation of higher performance devices. Examples include: powerful sonar, ceramic phono cartridges, piezo ignition systems, sonobouys, small sensitive microphones, and ceramic audio tone transducers (Piezo Systems 2002).

More recently piezoelectrics have been replacing solenoids in actuation systems. Automotive fuel injectors have been developed using piezoelectrics. The large forces developed by piezoelectrics make them the ideal selection for actuation of high pressure direct injection fuel injectors. Piezoelectrics have been successfully integrated into pumps. Composites can be manufactured with embedded piezos, creating a surface that can morph under applied electric fields.

2.2 Mechanics of Piezoelectric Material

Piezoelectricity is a property of select crystalline materials that produce strain in the presence of an electric field and electric charge when subject to stress. Ferroelectric materials are a subclass of piezoelectricity. Ferroelectrics only exhibit the piezoelectric effect after subjected to large external electric fields, known as the coercive field. The process, known as poling, orients the random polarization into a single crystallographic direction due to an applied electric field larger than the coercive field. A graphical depiction of the poling process of a piezoelectric ceramic is shown in Figure 2.2.1.

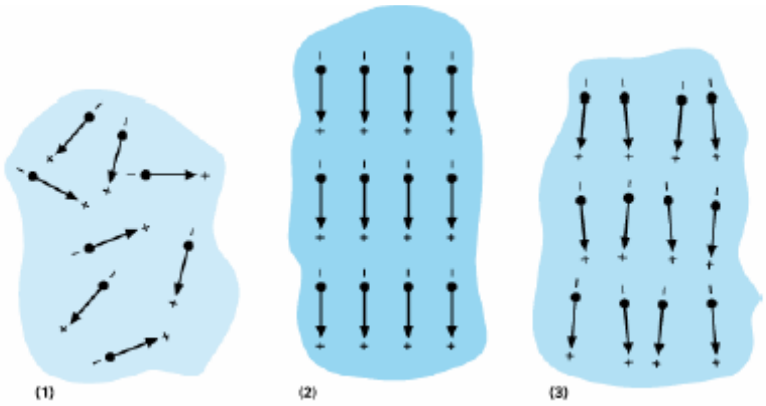

Figure 2.2.1: Ceramic Polarization: (1) before poling, (2) during poling and, (3) after poling (Physik Instrumente 1996)

It is important to notice that once the ceramic is poled and the electric field is removed all the dipoles do not align. This misalignment is due to the many different grains of the ceramic; there is misalignment of the crystallographic directions amongst the grains. The misalignment occurs during the fabrication stage. While the ceramic is being sintered, the individual grains rotate in order to minimize the total energy of the ceramic. In a piezoelectric single crystal the dipoles would align along a single crystallographic direction, since a single crystal is composed of a single grain.

The material behavior can be best understood through examining the behavior of a single unit cell. A unit cell of the most common piezoelectric material, lead zirconate titanate $Pb(Zr,Ti)O_3$, referred to as PZT is depicted in Figure 2.2.2. The concept of the Curie temperature, which is the temperature at which there is a change in the ferroelectric properties of a substance, is important in understanding piezoelectricity.

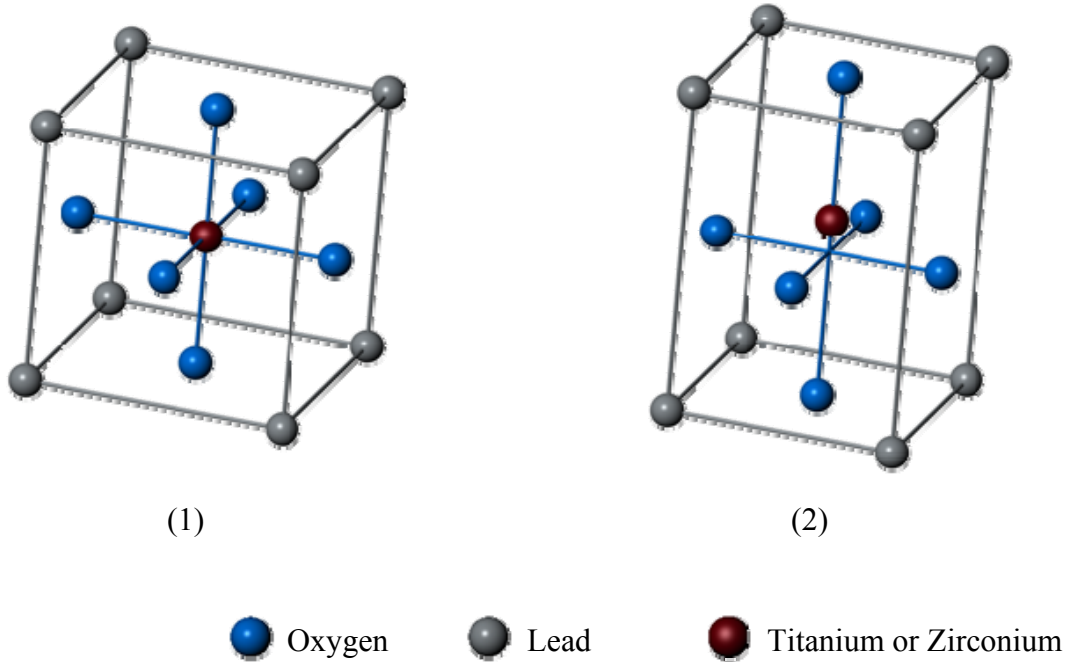

Figure 2.2.2: PZT unit cell (1) above Curie temperature and (2) below Curie temperature.

Above the Curie temperature, as shown in Figure 2.2.2, there is no shift of the central titanium or zirconium atom. The material is in the cubic phase. In the cubic phase, polarization is absent and the material is not piezoelectric. Below the Curie temperature, the material is in the tetragonal phase; the central atom is shifted toward one of the six face-centered oxygen atoms. This shift results in a dipole, created by the misalignment of the positively charged titanium or zirconium and negatively charged oxygen atoms. The direction of the central atom shift is determined by many factors on varying length scales. Locally affecting the direction is the orientation of neighboring dipoles and inter-granular stresses. Macroscopically, the applied stress and electric field also affect orientation.

In understanding the macroscopic material behavior, when subject to electrical and mechanical loads, it is beneficial to examine the behavior of a single unit cell, shown in Figure

2.2.3. In Figure 2.2.3(1) the polarization, *P*, and the applied electric field, *E*, are aligned and the result is a larger polarization, an elongation of the unit cell in the direction of the polarization, and a transverse contraction, shown in Figure 2.2.3(2). This behavior is know as the converse piezoelectric effect and is utilized by piezoelectric actuators. The polarization can be reoriented by applying an electric field larger than the coercive field in the opposite direction of the polarization, a process known as ferroelectric switching, shown in Figure 2.2.3(3) and (4). Applying a compressive stress, larger than the coercive stress, aligned with the polarization will produce a ferroelastic switch, depicted in Figure 2.2.3(5) and (6). The direction of the polarization following a ferroelastic switch can be any of the four possible directions transverse to the original poling direction. Both ferroelectric and ferroelastic switching creates non-linearity in the material behavior.

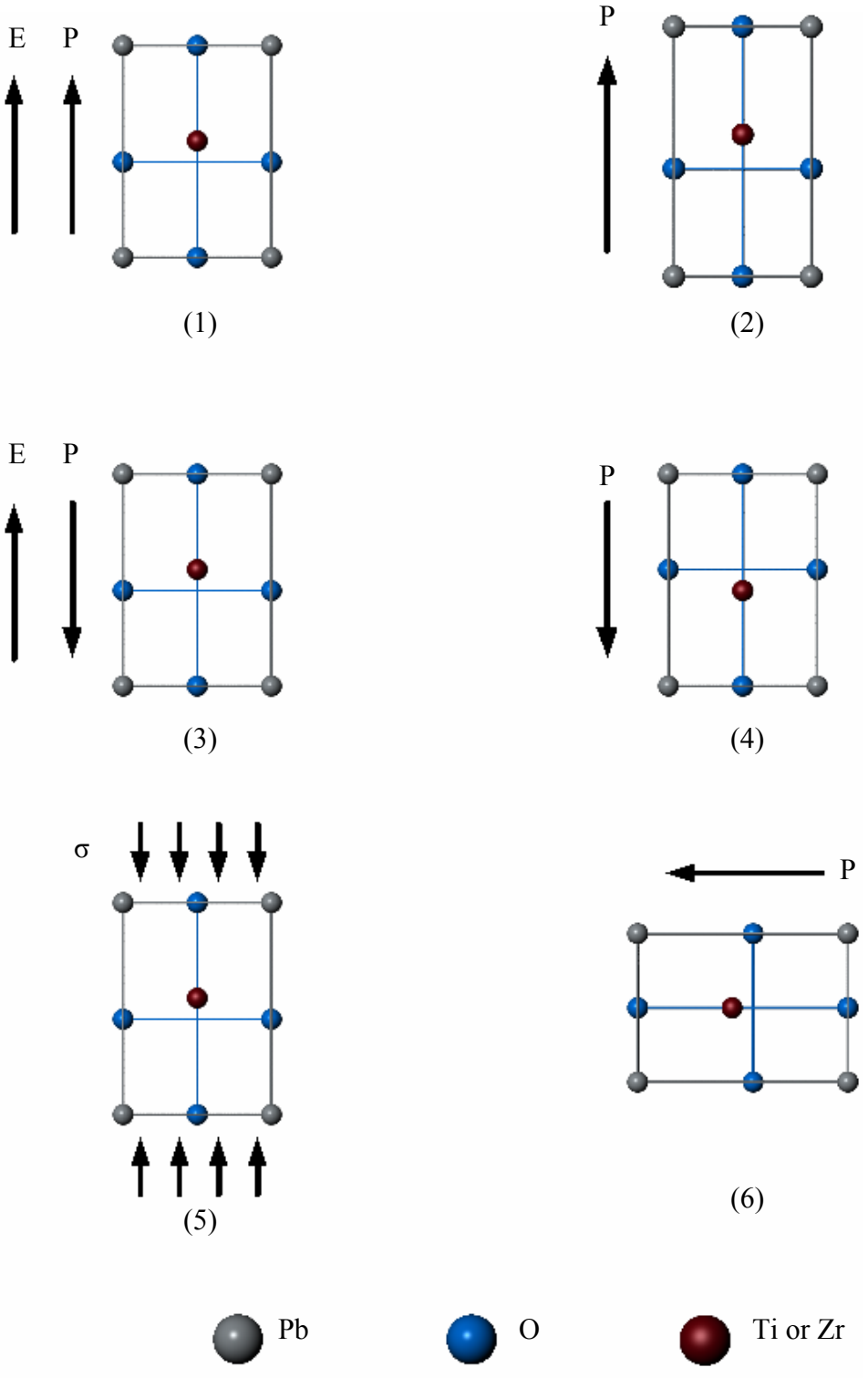

Figure 2.2.3: Unit cell response to electrical and mechanical loading

The presence of polarization creates complexities, such as anisotropy and hysteresis, when analyzing material behavior. The material properties of PZT are transverse isotropic about the poling axis. Since piezoelectric materials are not isotropic, the material coefficients are characterized on three principal directions. The "3" direction is selected to coincide with the poling axis. Directions "1" and "2" are transverse to the poling axis and have the same material coefficients, since the material is transverse isotropic. Piezoelectric materials are characterized in terms of four variables: stress, strain, electric field, and electric displacement.

Electric displacement, D, is related to the polarization, P, the permittivity of free space, ε_0 (=8.85 x 10^{-12} C/V-m) and, the applied electric fields, E, by Equation(2.2.1).

$$D_i = P_i + \varepsilon_0 E_i \tag{2.2.1}$$

For most piezoelectrics, the numerical value of the second term on the right hand side of Equation (2.2.1) is very small and is neglected, thus polarization and electric displacement become interchangeable. Figure 2.2.4 (Lynch 1996) is a plot of the electric displacement vs. the applied electric field, called the D-E hysteresis loop, for a lanthanum doped PZT, called PLZT. Point A in Figure 2.2.4 corresponds to the remnant polarization of the specimen, which is defined as the polarization present under no applied electric field, and equals 0.25 C/m^2. At point B the specimen has reached the negative coercive field and the polarization begins to switch. All of the dipoles have switched at point C. The specimen has the same behavior under a positive electric field, only the direction of the applied electric field and polarization are opposite from the process previously described, shown in points D through F. In applications, the material typically operates in the almost linear region between points A and F.

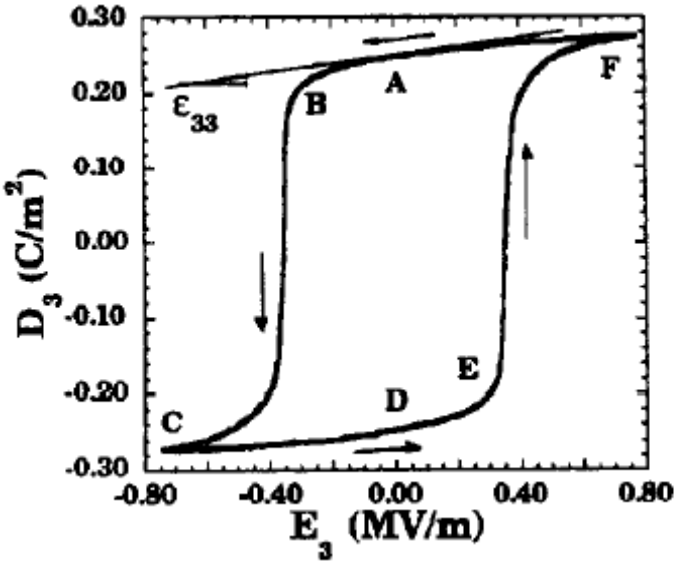

Figure 2.2.4: D-E hysteresis loop for PLZT (Lynch 1996)

The strain - electric field behavior is important when developing actuators. A strain – electric field plot is shown in Figure 2.2.5 (Lynch 1996).

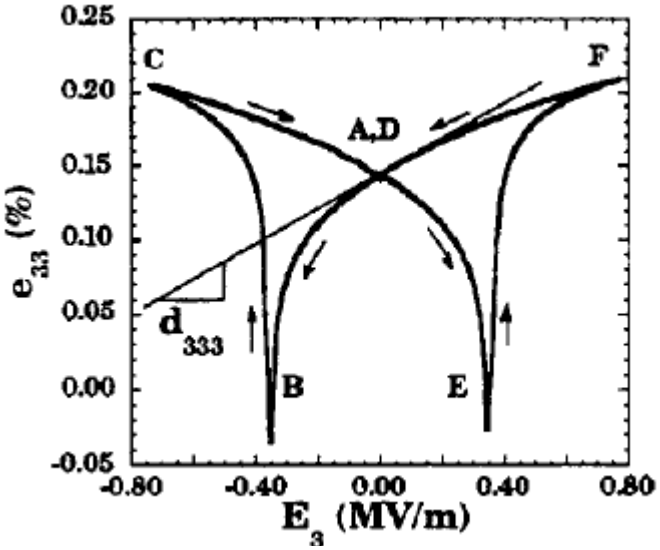

Figure 2.2.5: Strain – electric field hysteresis loop for PLZT (Lynch 1996)

Point A corresponds to the remnant strain in the material, a consequence of the remnant polarization. As a negative electric field is applied, the material shrinks in the longitudinal

direction until the coercive field is reached at point B. At B the polarization begins to switch (ferroelectric switching, described earlier in Figure 2.2.3(3)-2.2.3(4)) such that its direction coincides with the electric field. At point C the polarization has finished switching and the electric field starts becoming more positive which again causes the material to shrink. The strain decreases until the positive coercive field is reached at point E, at which the polarization switches again. In applications the material operates between points A and F.

Ferroelastic switching causes non-linearity in the stress - strain behavior as shown in Figure 2.2.6 (Lynch 1996).

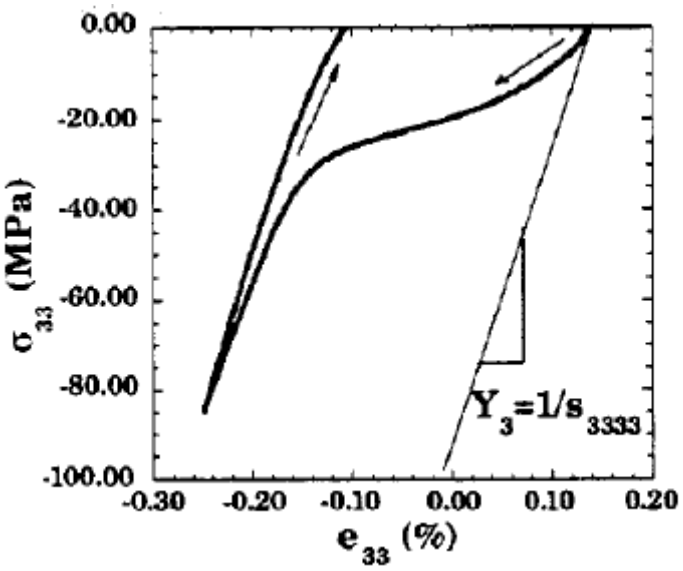

Figure 2.2.6: Stress – strain behavior for PLZT (Lynch 1996)

PLZT is a soft piezoelectric, which means it is easily depolarized by stress. Shown in Figure 2.2.6, ferroelastic switching occurs at a low stress level, as evident by the change in slope. Once the entire material has switched, linear elastic material behavior is observed.

In applications, switching behavior is undesirable because it can lead to cracking of the piezoelectric material and self-heating. For the most part, piezoelectric materials are operated in

the region around the remnant state. This region is nearly linear and constitutive models have been created to predict the material response to external loading.

2.3 Constitutive Behavior

A constitutive model for piezoelectric materials has been developed. The model is based upon the concept of linear piezoelectricity. In which the elastic, piezoelectric, and dielectric coefficients are treated as constants independent of the magnitude and frequency of applied mechanical stresses and electric fields (ANSI/IEEE Std 176-1987). The mechanical and electrical losses are neglected. These constitutive relations are shown in Equations (2.3.1) through(2.3.4).

$$T_{ij} = c^{E}_{ijkl} S_{kl} - e_{kij} E_k \tag{2.3.1}$$

$$D_i = e_{ikl} S_{kl} + \varepsilon^{S}_{ik} E_k \tag{2.3.2}$$

$$S_{ij} = s^{E}_{ijkl} T_{kl} + d_{kij} E_k \tag{2.3.3}$$

$$D_i = d_{ikl} T_{kl} + \varepsilon^{T}_{ik} E_k \tag{2.3.4}$$

Where T_{ij} is the stress component, C_{ijkl} is the elastic stiffness, s_{ijkl} is the elastic compliance, S_{kl} is the strain component, e_{kij} is the piezoelectric stress constant, E_k is the electric field component, D_i is the electric displacement, d_{kij} is the piezoelectric strain constant, and ε_{ik} is the dielectric permittivity. The superscripts E and S signify material properties measured at constant electric field and strain respectively. The subscripts i, j, and k are used to represent the three orthogonal directions 1, 2, and 3. As a matter of convention the "3" direction is chosen to align with the poling direction.

2.4 Single Crystal Piezoelectrics

Single crystal piezoelectrics possess superior piezoelectric properties when compared with their ceramic counterparts, such as PZT. Two common single crystal materials are PMN-PT and PZN-PT. The d_{333} piezoelectric strain coefficient for single crystal materials is 1800-2000 pC/N compared with 400-750 pC/N for a PZT ceramic, meaning single crystals will produce roughly three times the strain of a ceramic under the same electric field. Single crystals will produce a lower blocked force than an equally sized ceramic due to a lower elastic stiffness. Even with the blocked force reduction, the energy density is greater for a single crystal, making them ideal for high performance devices.

Another benefit of single crystals is they exhibit far less hysteresis in their electromechanical response. This translates in far less self-heating when driven at high frequencies in actuator applications, compared with conventional PZT ceramics.

A drawback to the use of single crystals in devices is that they are prone to cracking under the combined loading of temperature, stress, and electric field. Much of this cracking behavior has been attributed to a phase transformation. Material research has developed an energy based model to predict this phase transition. An understanding of the underlying material behavior will bring about the successful incorporation of single crystals into actuators.

2.5 Piezoelectric Actuators

2.5.1 Piezoelectric Benders

Piezoelectric benders consist of a layer of piezoelectric material, which is poled through the thickness, bonded to a substrate. When an electric field is applied, the piezoelectric material

will exhibit a positive strain in the thickness direction; a negative strain is produced in directions orthogonal to the thickness. This behavior is analogous to the elastic Poisson effect and is referred to as the d_{311} behavior, since the electric field is applied in the x_3 direction and the strain is measured in the x_1 direction. Since the piezo is constrained at the interface with the substrate it can not contract as a result of the d_{311} behavior, thus a tensile stress is created in the piezoelectric material. Equilibrium dictates that there will be an equal and opposite compressive force in the substrate to balance the tensile force in the piezo. These equal and opposite forces create a moment, which induces curvature in the bender. By cantilevering one end of the bender, the opposite end will translate in one direction as a result of the curvature introduced by the applied electric field. Such an actuator is known as a unimorph, since it can produce motion in one direction. A bimorph is created by bonding piezoelectric materials on both sides of the substrate. By actuation each side independently the bender can produce motion in both directions.

Benders now a commercially available product and their inherent displacement amplification technique make them suitable for use in devices. The drawback to using benders is they rely solely in the d_{311} behavior, which is roughly a third of the d_{333} response. Therefore a more efficient actuator can be obtained by using the d_{333} behavior.

2.5.2 Piezoelectric Stacks

Piezoelectric stack actuators consist of many thin layers of piezo stacked with electrodes between the layers. Strain is proportional to the applied electric field and by decreasing the thickness of the layers the same electric field can be achieved using less voltage. By stacking many layers, the displacements of each layer will add together to form an output that is usable in

a device. Since each layer is sandwiched by electrodes, the stack makes use of the d_{333} behavior, i.e. the applied electric field and strain are in the same direction.

Piezoelectric stacks come in many varieties. Initially the individual layers of ceramic were cut from a block of material, electrodes were plated on the top and bottom, and the layers were glued together. Stacks made using this process had layer thicknesses of 0.25mm to 0.5mm which would require drive voltages of 500V and 1000V respectively. More recently stacks are able to be produced with layer thickness of 20 μm, resulting in drive voltages of 40V. These stacks are made by a co-firing process. A thin, ~20 μm, layer of the "green" or unfired ceramic paste is laid down and an electrode is screen printed on top of the layer. This is followed by another layer of ceramic and another electrode. Layers are stacked in this manner until the desired height is reached, where the entire assembly is baked to produce the stack. Since there is no ceramic cutting or human handling prior to assembly, the layers can be made very thin. A consequence of the increased number of layers is the capacitance also increases, which requires larger currents when operated at high frequencies in devices. Both co-fired and hand assembled stacks are commercially available from numerous companies and have been incorporated into commercial products such as automotive fuel injectors.

CHAPTER 3: LITERATURE REVIEW

3.1 Motivation for a Helicopter Main Rotor Trailing Edge Flap

Placing a trailing edge flap on a helicopter main rotor can serve two purposes. The first is to suppress blade vibrations and aerodynamic interactions between blades. The second purpose is to perform primary flight control functions.

Helicopters rotor and subsequently the airframe experience high vibration levels due to the unsteady aerodynamic environment they operate in. These vibrations are undesirable because of the high stresses imposed upon the rotor blades which is transferred the airframe. Also the vibrations and blade-vortex interactions create acoustic noise which is unfavorable in the creation of silent and stealthy military helicopters.

It has been shown that higher harmonic control (HHC), where the blade pitch is excited at frequencies that are integer multiples of the blade's rotational rate, can reduce the vibration level present in a helicopter. Later it was found that individual blade control (IBC), allowing each individual blade to be driven at any desired frequency, was a further improvement upon HHC. Initially IBC required a complicated hydraulic slip ring and pitch link assembly and as a result incurred a substantial weight penalty (Ben-Zeev and Chopra 1996). The desire to achieve IBC has lead into the use of embedding smart materials, such as piezoelectrics, in the blade.

Conventional flight control systems of helicopters are extremely complex. "They generally have numerous exposed linkages, bearings, swash plates, push rods, and hinges. These components are maintenance intensive, costly, and act as a significant source of drag. The

basic swash plate control concept was invented in the 1930s and is overall a successful design" (Chopra and Shen 2004). The aforementioned shortcomings of a conventional helicopter control system warrant the search for a new flight control solution using advanced materials and construction techniques.

3.2 Previous Designs

3.2.1 Unimorph and Bimorph Benders

Researchers working at the Massachusetts Institute of Technology (M.I.T) developed the first piezoelectric driven trailing edge flap, utilizing a bimorph bender actuator. The design used a long piezoelectric beam consisting of two PZT plates bonded on either side of a metal substrate. The piezoelectric beam was cantilevered inside the airfoil. Actuating the PZT on one side of the beam would cause the beam to deflect toward the side actuated. The tip of the piezoelectric beam was attached to the trailing edge flap using a small linkage with nylon hinges. The linkage coupled the motion of the beam to the trailing edge flap. A schematic of the design can be seen in Figure 3.2.1.

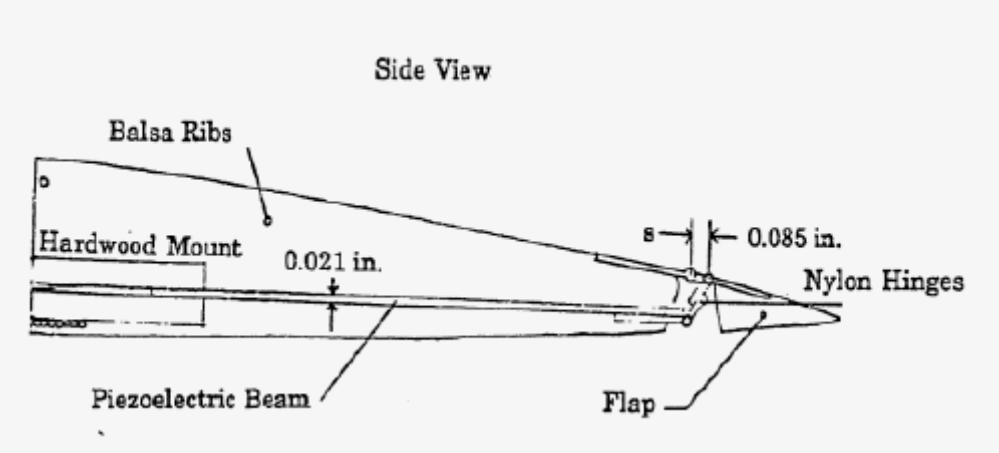

Figure 3.2.1: Schematic of an early M.I.T. design (Spangler 1989)

The focus of the study was to evaluate the flaps performance in an aeroelastically scaled physical environment. The three measures of performance were the flap deflection, change in lift, and change in moment due to the flap. The system was tested under a range of electric fields, airspeeds, and excitation frequency.

When the piezoelectric elements were driven at 8.8V/mil the flap produced 5.2 degrees of free deflection, which is much less than the 16.3 degrees predicted by their theoretical model. When the air foil was subjected to a wind speed of 23.8 m/s the flap deflection was 3.8 degrees compared with the predicted 11.9 degrees. The difference in theoretical and actual performance was attributed to nonlinearities, such as friction and backlash, introduced by the hinges (Spangler 1989).

In order to improve the performance of the trailing edge flap, modifications were made to the design. The hinges were replaced by flexures, which eliminated problems with friction and backlash. The second improvement is the use of a tapered thickness bender. The tapered thickness offered improvements in bender efficiency, inertia and size properties (Prechtl 1994). A schematic of the design is shown in Figure 3.2.2.

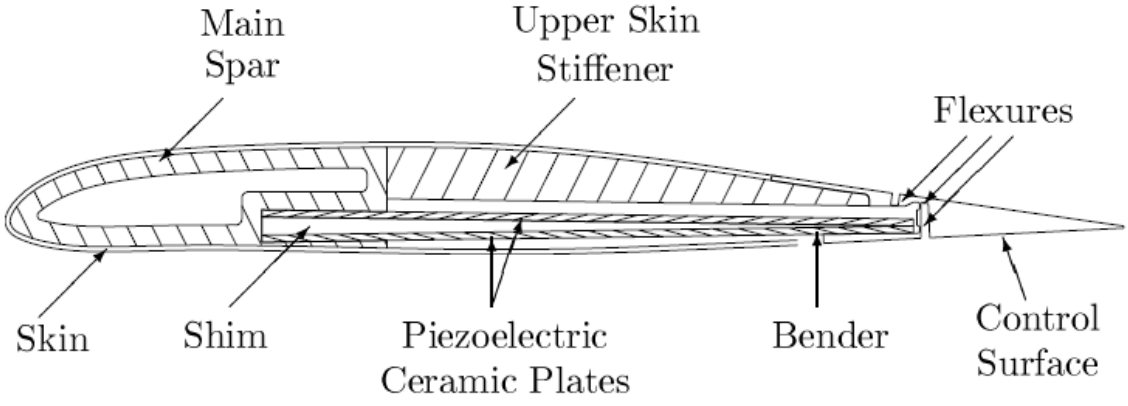

Figure 3.2.2: Schematic an improved M.I.T. design (Prechtl 1994)

This design was not tested under aeroelastic loads, but it produced 11.5 degrees of flap deflection at 10 Hz. The improved design was driven with higher electric field levels, 40 V/mil compared with the 8.8 V/mil used in the previous design. Much of the increased system performance can be attributed to the increased electric field level.

In addition to the work performed at M.I.T. several other researchers have produced trailing edge flaps driven by piezoelectric bender elements. Oren Ben-Zeev and Inderjit Chopra from the University of Maryland also produced a design utilizing a bimorph bender with mechanical linkages and hinges to couple the motion from the piezoelectric elements to the flap. They highlight that the drawback to using bender elements is that they are incapable of producing both large forces and displacements (Ben-Zeev and Chopra 1996). As mentioned previously, piezoelectric benders operate using the d_{311} mode, which is an indirect material effect, similar to the Poisson effect in elastic materials. For typical piezoelectric ceramics the d_{333} piezoelectric coefficient is usually three times larger than d_{31}, meaning that exploiting the d_{333} mode will produce roughly three times the work of the d_{311} mode. This phenomenon lead researches to develop trailing edge flap designs utilizing the d_{333} mode of actuation.

3.2.2 Stack Actuator Designs

Leveraging on their previous experience developing trailing edge flaps using piezoelectric benders, researchers at M.I.T. developed an actuator design utilizing piezoelectric stacks, called the X-frame. The small displacements of the piezoelectric stacks are amplified by the X-frame. Figure 3.2.3 shows a simple truss model that depicts the operation of the actuator.

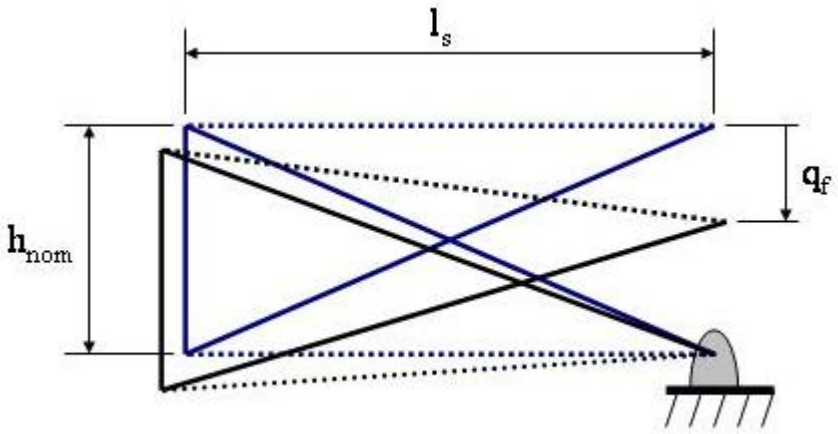

Figure 3.2.3: Simple Model of X-frame Actuator

The blue and black lines represent the initial configuration and actuated configuration respectively. The dotted lines depict the location of the piezoelectric stacks. The free displacement of the actuator, q_f, is a function of the length of the stacks, l_s, the stack spacing, h_{nom}, and the piezoelectric strain, ε. The formula for free displacement is given by Equation(3.2.1).

$$q_f = -\frac{2l_s}{h_{nom}}\left(1+\frac{\varepsilon}{2}\right)(\varepsilon l_s) \tag{3.2.1}$$

An isometric view of the actuator can be seen in Figure 3.2.4.

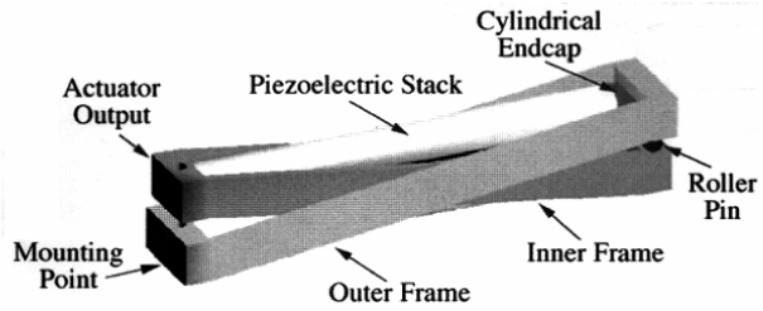

Figure 3.2.4: Isometric view of the X-frame actuator (Prechtl and Hall 1999).

The prototype device used cylindrical stacks 3.094" long and a diameter of 0.315" and was able to produce ~0.085" linear free displacement and a blocked force of ~55 lbs (Prechtl and Hall 1999).

A collaboration under the DARPA SMART Rotor Program involving Boeing, M.I.T., The University of Maryland and, The University of California: Los Angeles, continued development on the X-Frame Actuator. The final version of the actuator, called the 2x-Frame, used two X-frame actuators operated in a push-pull configuration, was able to develop a blocked force of 113lb. and a free displacement of 0.081 in. The culmination of the effort was a full scale whirl tower test of five MD900 helicopter blades modified to include a trailing edge flap and 2x-frame actuators, shown in Figure 3.2.5.

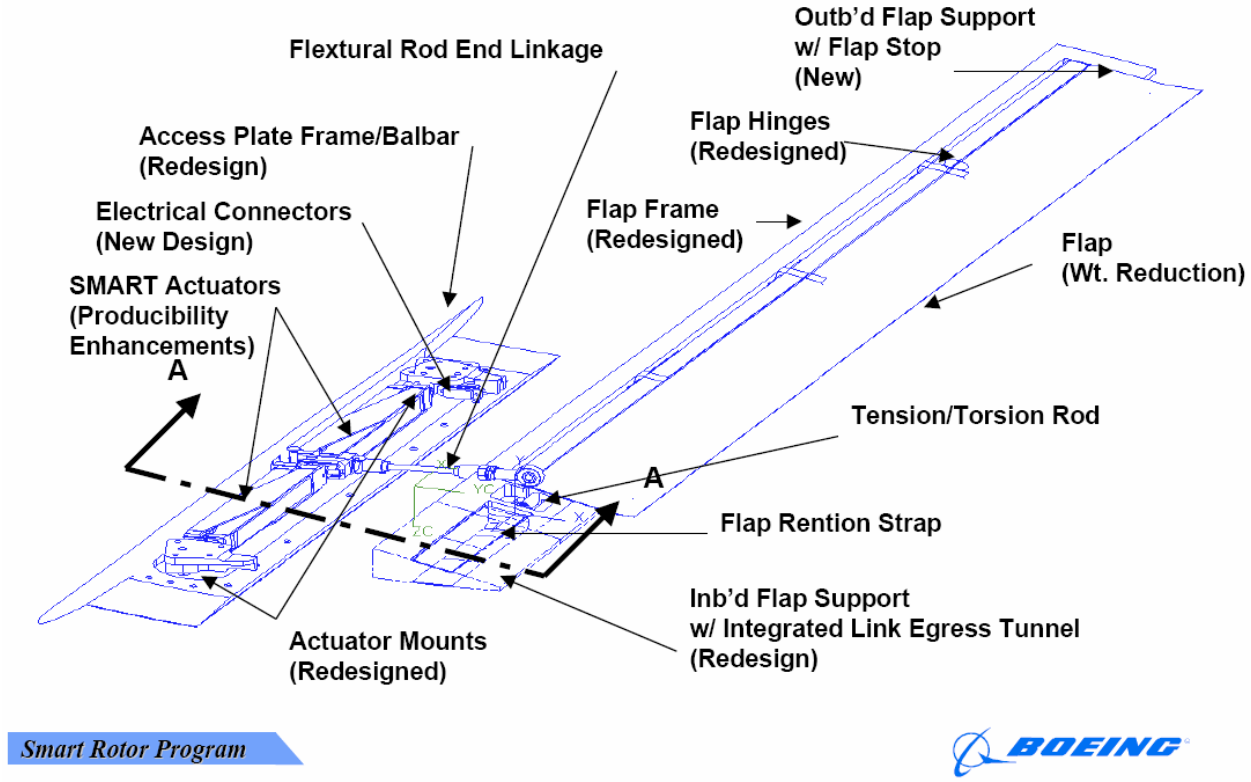

Figure 3.2.5: Dual X-Frame and trailing edge flap configuration (Straub and Derham 2000)

Simulations and model scale wind tunnel test show the system can provide 80% vibration reduction and 10dB noise reduction. The dual X-Frame actuator amassed over 60 million cycles during the bench testing phase. During the full scale whirl tower test the rotor was tested for 13 hours, which include 7 hours of flap operation, two of which were continuous. At full rotor speed, 392 RPM, the actuator produced a flap displacement of 3.4 degrees and increased the rotor thrust by 575 lbs, when actuated at a frequency of 5/rev. Testing also included limited closed loop vibration control and effects of a single actuator failure on rotor loads and vibration levels (Straub, Kennedy et al. 2004).

CHAPTER 4: CONCEPTUAL ACTUATOR DESIGN

4.1 Design Objectives

The objective was to develop a proof-of-concept, piezoelectric driven actuator suitable for driving a trailing edge flap on the main rotor of a helicopter. The actuator developed at this stage was not required to fit the size and weight constraints of being mounted in a helicopter blade, but was scalable in order to do so. A goal was to use off-the-shelf components as much as possible to minimize fabrication time. Primarily, the actuator assembly was developed using PZT actuators as the driving elements, due to their availability and cost. The device was capable of being converted to use single crystal driving elements, with minimum modifications.

4.2 Design Requirements

The proof-of-concept actuator developed in this study differs from a flight-worthy actuator in the requirements of size, free displacement, and blocked force. The size of the proof-of-concept was dictated by the size availability of off-the-shelf components. The free displacement and blocked force are dependent on the amount of piezoelectric materials used and the mechanical amplification ratio.

The design requirements for a flight-worthy actuator are listed below in Table 4.2.1 (Straub, Ngo et al. 2001). The free displacement value listed in Table 4.2.1 will produce ±2º of flap deflection, necessary to provide vibration suppression, using a 0.75 in. control horn attached to the flap.

Table 4.2.1: Design requirements for a flight-worthy trailing edge flap actuator

Requirement	**Objective**
Force	28 ± 43 lb
Displacement	±0.032 in.
Bandwidth	0 – 40 Hz
Radial Acceleration	655 g
Flapwise Acceleration	29 g
Chordwise Acceleration	3 g
Temperature	-60 – 160 ºF
Humidity	up to 100% RH

The design requirements for the proof-of-concept actuation are listed in Table 4.2.2. The force and displacement requirements were selected to be different from the flight-worthy requirements. A goal for this study was to push the limits of piezo displacement amplification to support future designs.

Table 4.2.2: Design requirements for proof-of-concept trailing edge flap actuator

Requirement	**Objective**
Force	5 lb.
Displacement	0.125 in.
Bandwidth	0 – 40 Hz

4.3 Conceptual Design

A design utilizing both mechanical and hydraulic amplification was developed. A schematic for the design developed is shown in Figure 4.3.1.

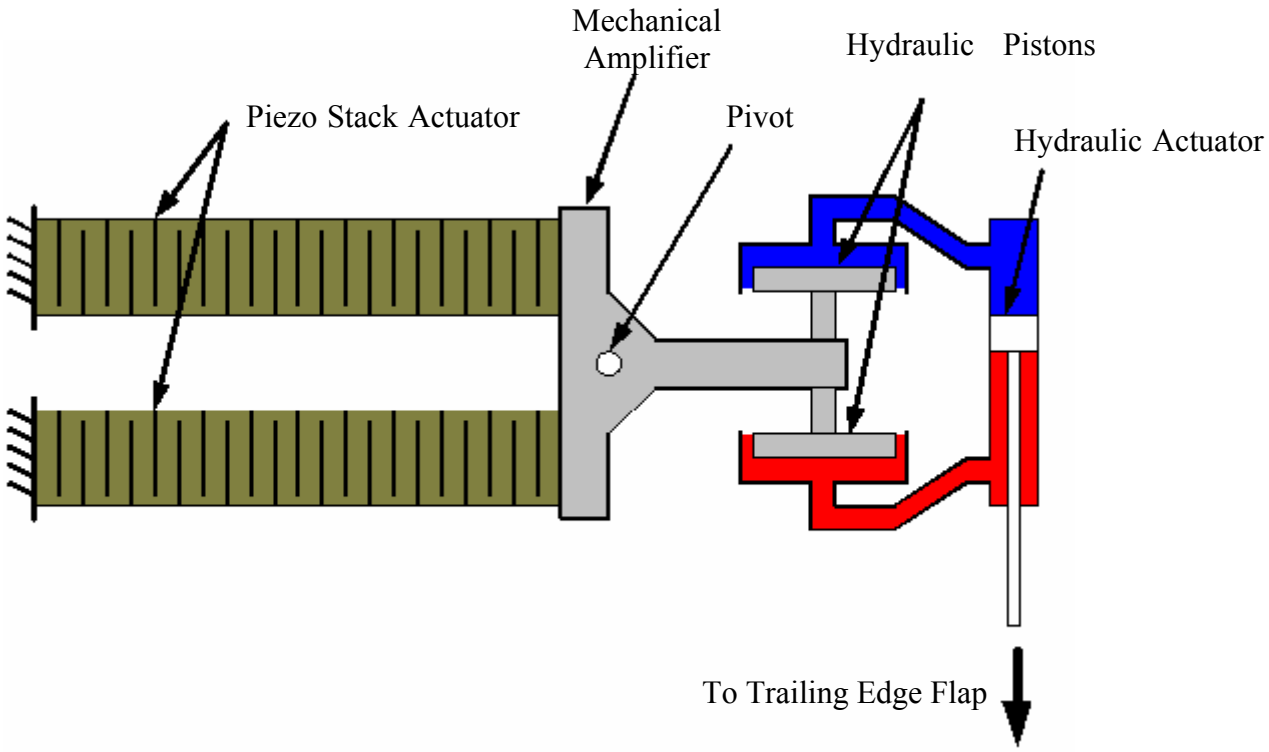

Figure 4.3.1: Schematic of Conceptual Design

The two piezoelectric stack actuators operate antagonistically, or 180º out of phase, acting upon the mechanical amplifier, which is referred to as a rocker, causing a cyclic rotation of the rocker about the pivot. The rocker amplification is determined by the ratio of the output to input lever arm length. The output stage of the rocker is connected to two pistons. The pistons are part of a hydraulic amplification circuit, which includes a hydraulic cylinder that is attached to the trailing edge flap. The hydraulic amplification is determined by the ratio of the areas between the pistons and the hydraulic actuator. The design consists of three main subsystems, the piezoelectric stacks, the mechanical amplifier, and the hydraulic amplifier.

4.3.1 Piezoelectric Stacks

The design is based around the EPCOS co-fired PZT stacks. A picture of the EPCOS stacks is shown in Figure 4.3.2:

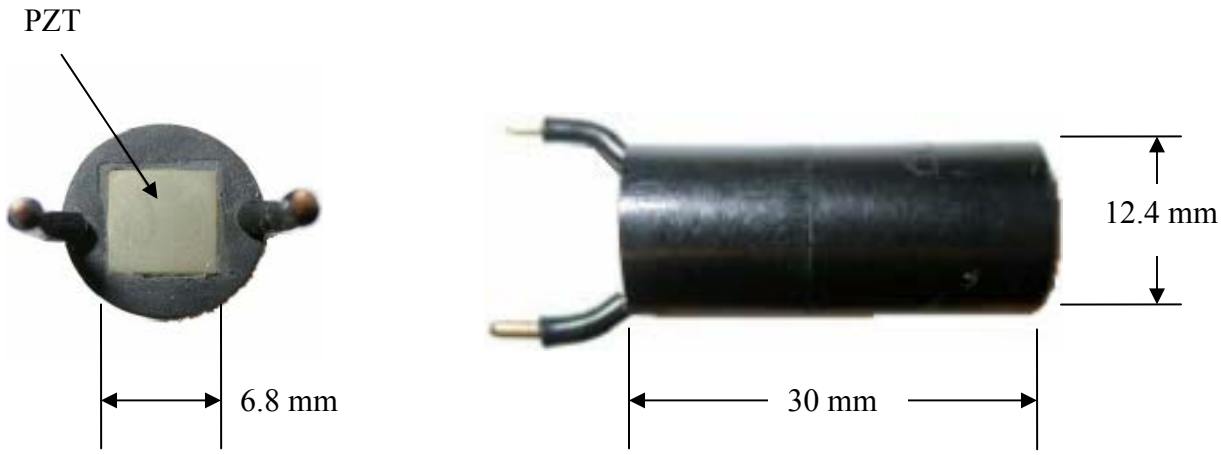

Figure 4.3.2: EPCOS co-fired PZT stack actuator

The EPCOS stacks extend 40µm under an electric field of 2 MV/m, which corresponds to a strain level of 1333 micro strain. The layer thickness is 80µm, thus in order to achieve an electric field of 2 MV/m requires a drive voltage of 160V.

To increase the systems output three stacks were bonded together as shown in Figure 4.3.2.

Figure 4.3.2: Picture of three bonded EPCOS stacks

In order to electrically isolate and distribute the forces between the stacks and other system components, small disks of alumina (shown in white in above picture) were bonded to the stacks. To decouple bending moments applied to the stacks, spherical washers were used on each end of the stack assembly. To further electrically isolate the stack assembly, heat shrink tubing was applied around the outside.

4.3.2 Mechanical Amplifier

A mechanical amplifier was developed to amplify the displacement of piezoelectric stacks. The piezo stacks act on each side of the pivot in order to balance the effect of thermal expansion. To produce a rotation of the rocker about the pivot point it is necessary for one stack to extend and the other to retract. Since piezoelectric stacks can not produce negative strain, both stacks are preloaded to half the peak applied electric field, and then the electric field increases on one stack while the other decreases. Thus, the applied electric field is 180 degrees out of phase between the two stacks.

The amplifier works on the principle of differential length lever arms as shown in Figure 4.3.3.

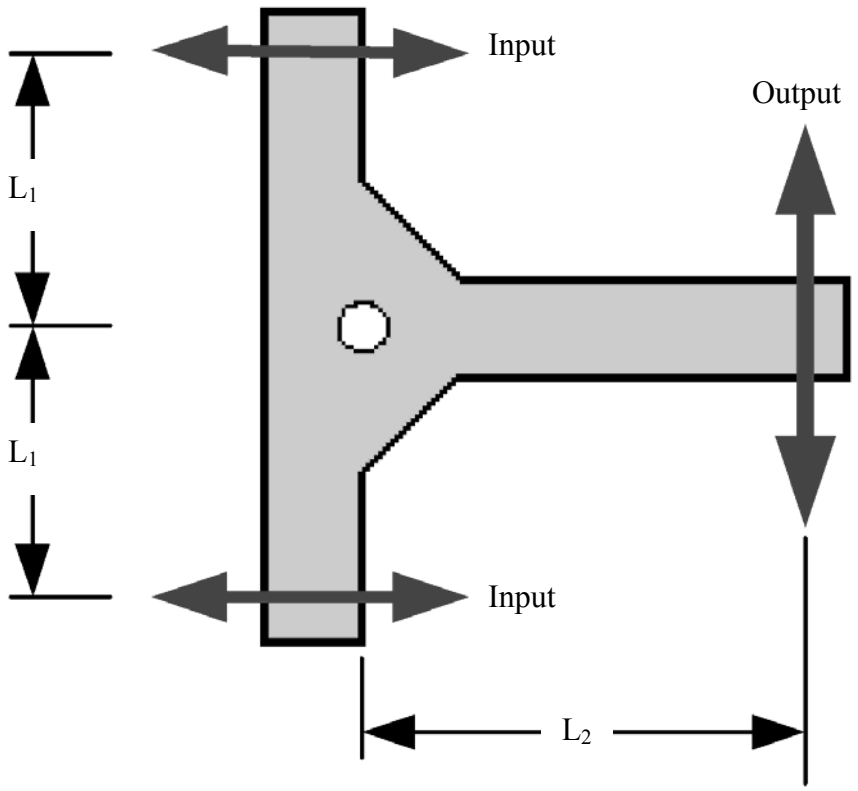

Figure 4.3.3: Mechanical Amplifier operation

The amplification factor is the ratio of output lever arm, L_2, to input lever arm, L_1. Since the displacement of the piezo stack actuators is small, 120 μm, the efficiency of the rocker is critical. The rocker must be free to rotate about the pivot without restrictions, which will require the use of a high quality ball bearing at the pivot. The rocker must also be sufficiently rigid, such that stack displacement is not absorbed by the elasticity of the rocker. Extensive finite-element analysis (FEA) was performed to ensure adequate rigidity.

4.3.3 Hydraulic Amplifier

A hydraulic amplifier was developed and coupled to the mechanical amplifier to further amplify the displacement of the piezoelectric stacks. The hydraulic amplifier has two pistons attached to the rocker, one on each side of the output stage. The pistons are connected to

opposite sides of a conventional hydraulic actuator. As the rocker rotates, one piston displaces fluid, causing a displacement of the hydraulic actuator. By selecting the area of the hydraulic actuator to be less than the area of the pistons, the hydraulic system will amplify the displacement of the mechanical amplifier.

To ensure overall system reliability and performance, proper sealing of the hydraulic subsystem and minimization of fluid compliance were determined to be critical parameters to the designs success. A rolling diaphragm seal was selected for the pistons attached to the rocker, similar to the one pictured in Figure 4.3.4.

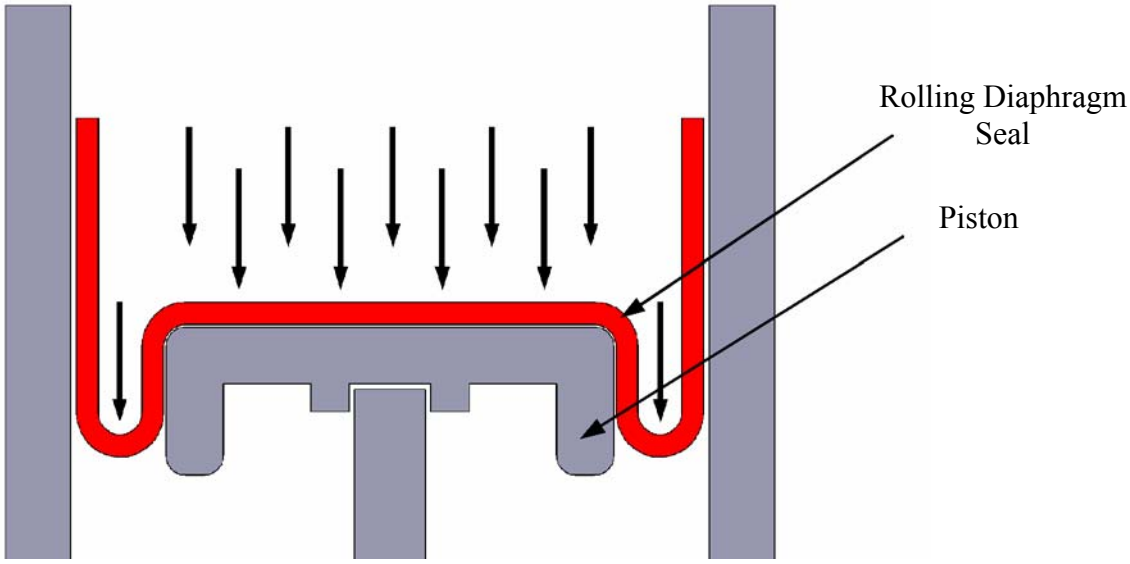

Figure 4.3.4: Schematic of Rolling Diaphragm Seal

The rolling diaphragm seal was chosen over other seals such as o-rings or cup seals due to several factors. The piston does not translate axially in the bore, but rather on a circular path, due to the rotation of the rocker. With sliding seals, such as o-rings and cup seals, there is usually some seal friction present that resists the motion. The piston stroke is small, 0.635mm (~0.025 in), therefore any inefficiency will dramatically reduce the system performance.

Equally important to system performance is the ability to remove any entrapped air from the hydraulic subsystem. Entrapped air can come from two sources. The most common source is air not removed during the bleeding process. Also air will dissolve into the hydraulic oil. To alleviate the problem of dissolved air, the fluid can be held under a vacuum before it is introduced into the system. The ability to circulate hydraulic fluid from the lowest system point to the highest will remove air during the bleeding process. After bleeding, application of a bias pressure to the hydraulic system will expand the seals and compress and/or collapse remaining air bubbles which will improve system performance.

4.4 Component sizing

The sizes of the mechanical and hydraulic amplifiers were chosen to achieve a large displacement output from the system. A consequence of the large displacement is the force output will be small. The values used to determine the theoretical system output are given in Table 4.4.1.

Table 4.4.1: Theoretical Actuator Performance

Stack Properties	
Cross Sectional Area	46.24 mm^2
Blocked Stress	25 MPa
Free Displacement	120 μm
Amplification Ratios	
Mechanical Amplification Ratio	5
Hydraulic Amplification Ratio	10.4
Total Amplification Ratio	**52**
System Output	
Calc. Free Displacement	6.24 mm
Calc. Blocked Force	22.23 N

The hydraulic amplification ratio was chosen based on the available sizes for commercially available hydraulic actuators and rolling diaphragm seals.

CHAPTER 5: CAD MODELS AND FINITE ELEMENT ANALYSIS

5.1 CAD Models

A full set of CAD models was developed in order to ensure an accurate fit between parts. The models were also used for finite element analysis (FEA) and exported to a computer aided machining program (CAM) for manufacture. Figure 5.1.1 is a picture of the entire assembly.

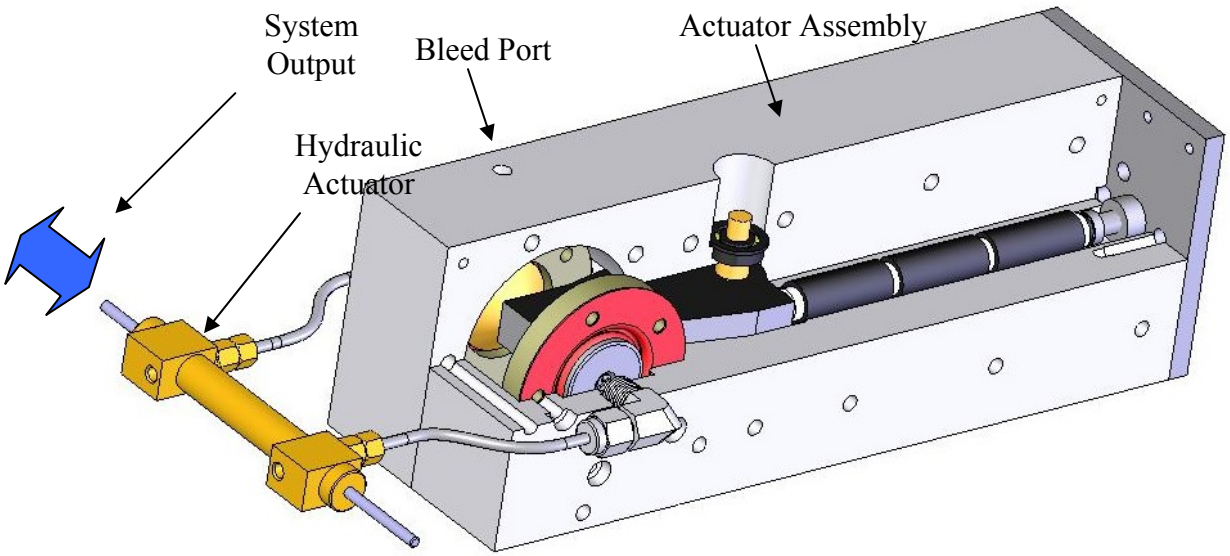

Figure 5.1.1: System Assembly (Partial Section View)

The majority of the design work was concentrated on the actuator assembly. A greater detailed view of the actuator assembly is shown in Figure 5.1.2.

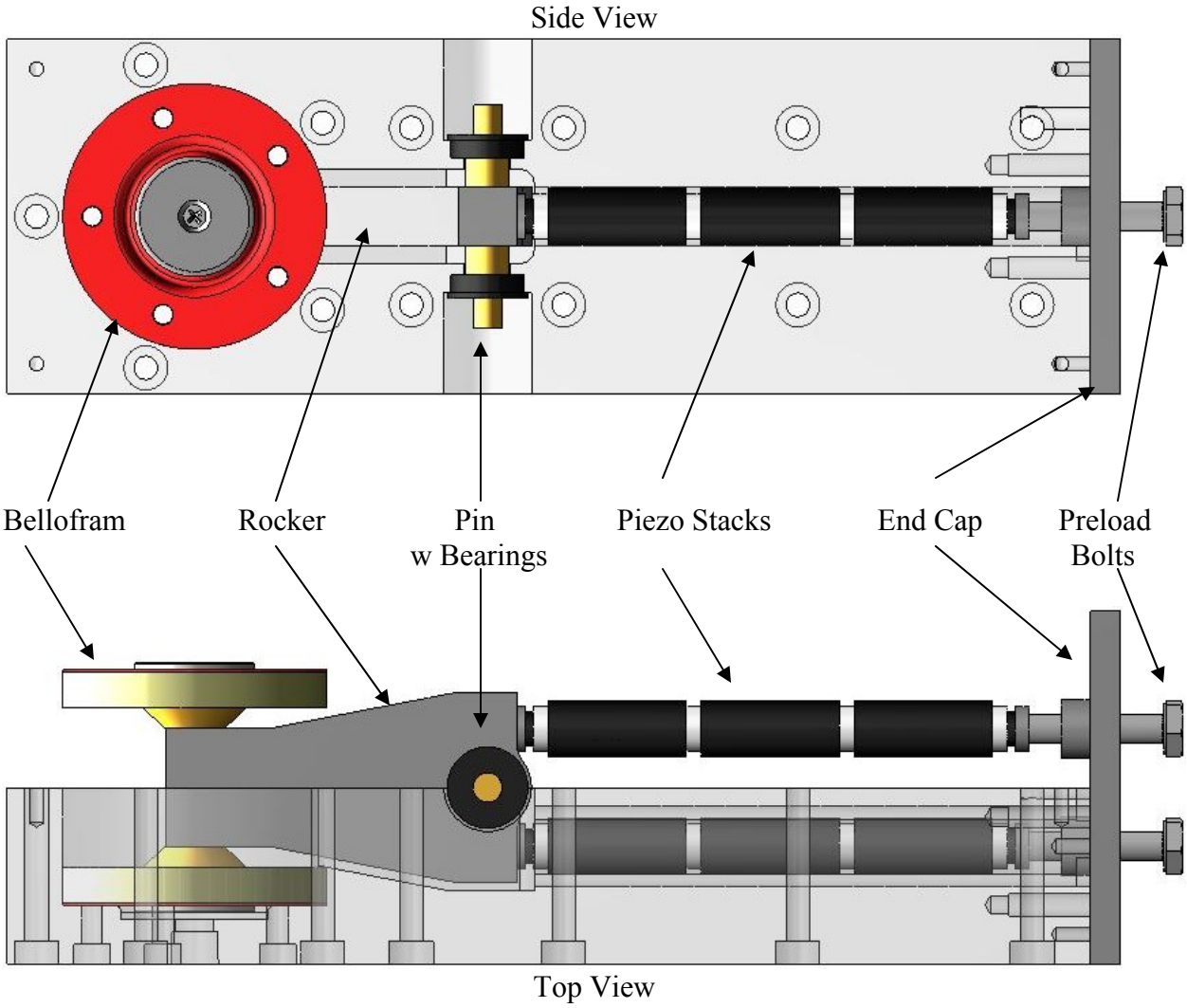

Figure 5.1.2: CAD actuator assembly (housing transparent)

One half of the housing is not pictured, while the other side is shown transparent for easier viewing of the working system components. The models and features of the individual parts are detailed in the subsequent sections.

5.1.1 Housing Assembly

The housing assembly consists of a left and right housing and an end plate. The left and right housings are mirror images of each other, with the exception of the fastening holes for attaching the housings together. The mounting holes on the right half have counter bores for the

socket head cap screws, while the left has 10-24 threaded holes. The right housing is shown in Figure 5.1.3.

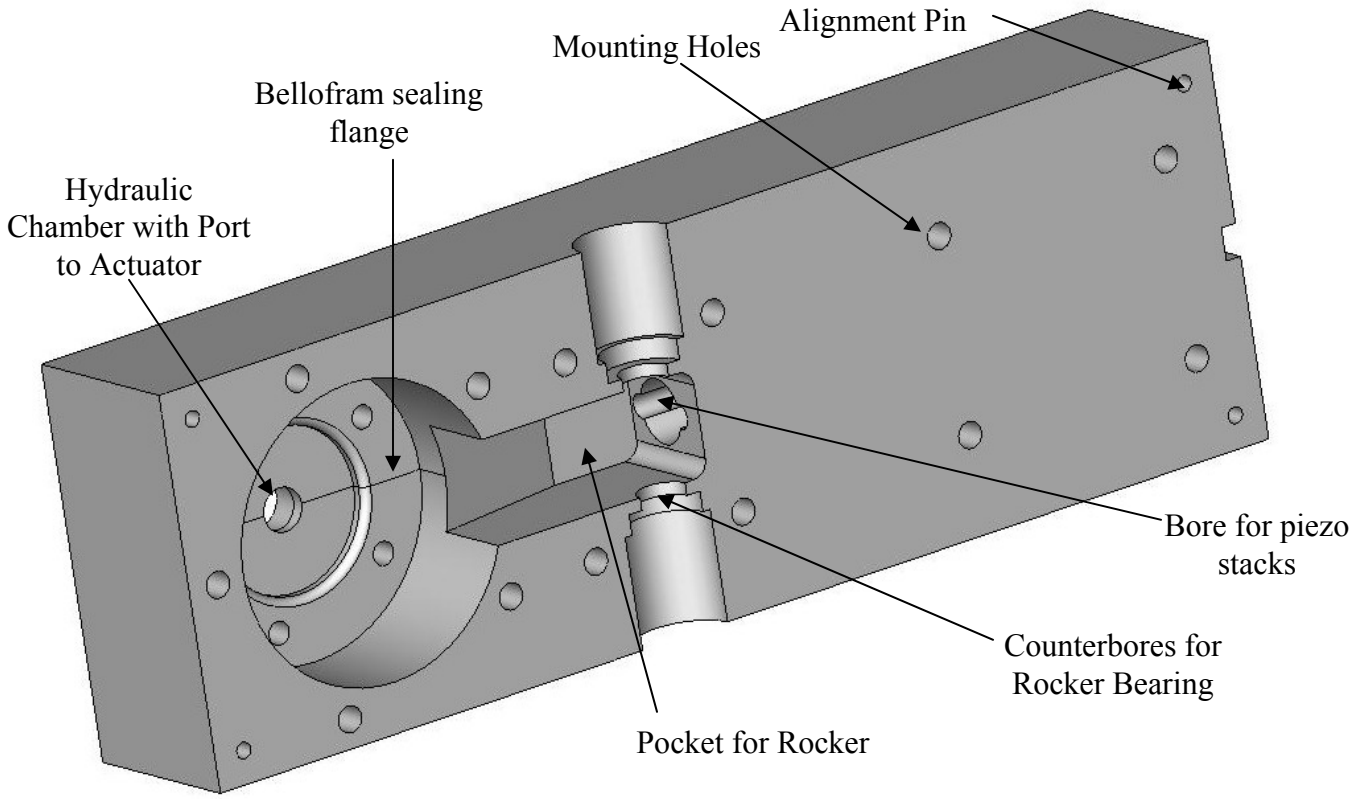

Figure 5.1.3: CAD model of right housing

The dimensions of the housings are 9 inches long by 1.5 inches thick by 3 inches tall and constructed of aluminum. The height of the actuator is fixed by the diameter of the belloframs. For the flight worthy actuator, custom seals will have to be developed in order to fit inside a rotor blade. The bore for the piezo stacks incorporate two channels for the power wires. A better view of the power wire channels is shown in Figure 5.1.4.

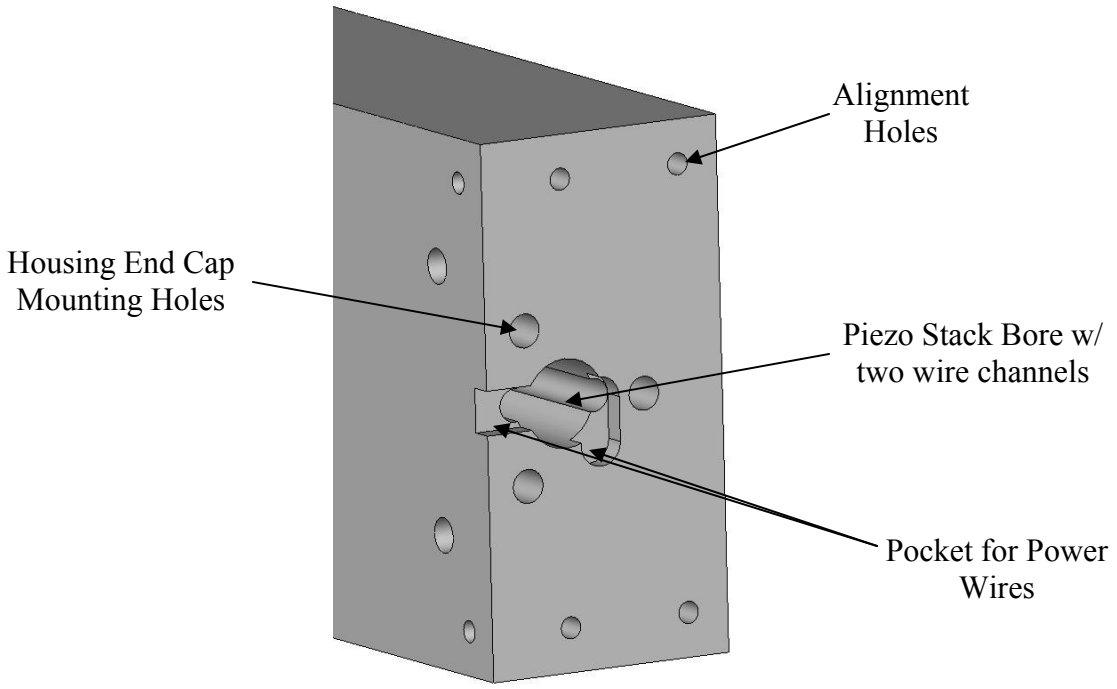

Figure 5.1.4: Detailed view of the end of the housing

A pocket is also machined into the end of the housing to allow the wires to pass from the channels to the holes in the housing end cap.

The housing end cap, which is made of steel, attaches to the housings using the mounting holes and alignment pins shown in Figure 5.1.5.

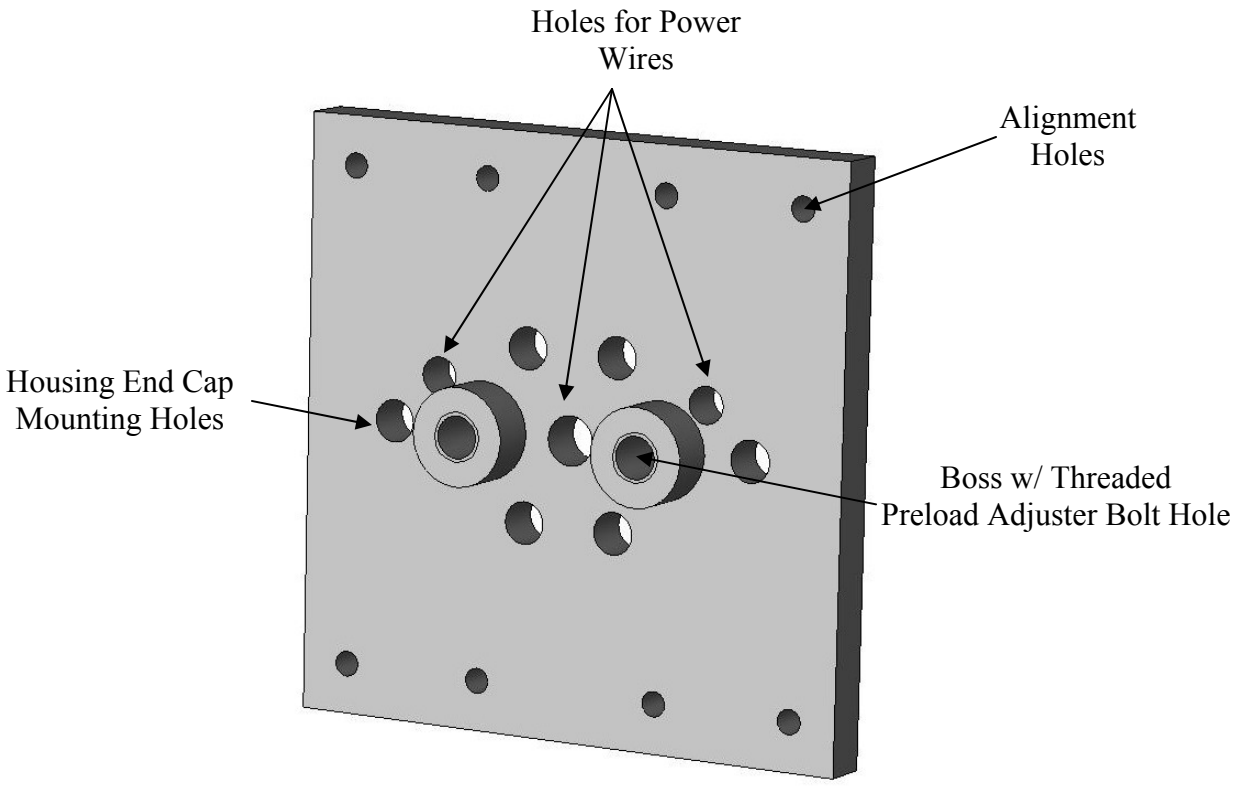

Figure 5.1.5: CAD model of housing end cap

The housing end cap also incorporates two threaded bosses for a bolts used to preload the piezo stacks. The holes for the power wires allow the ground wires from both sets of piezo stack to be passed through the end cap together using the center hole, while the positive wire for each set of stacks exit through their own individual holes. This helps avoid the possibility of electrical arcing between the two sets of wires.

5.1.2 Mechanical Amplifier

The mechanical amplifier consists of an aluminum rocker with a press fit steel pin. The rocker and pin rotated on two ABEC-7 bearings mounted to the left and right housings, as shown in Figure 5.1.6. The bearings allow the system to rotate freely, thus maximizing the overall system output. The rocker incorporates two small pockets, which accept the spherical bearings mounted to the end of the piezo stacks, forming the piezo actuation points. The pistons, which

are the coupling link between the mechanical amplifier and the hydraulic amplifier, are attached to the rocker using ¼”-28 set screws.

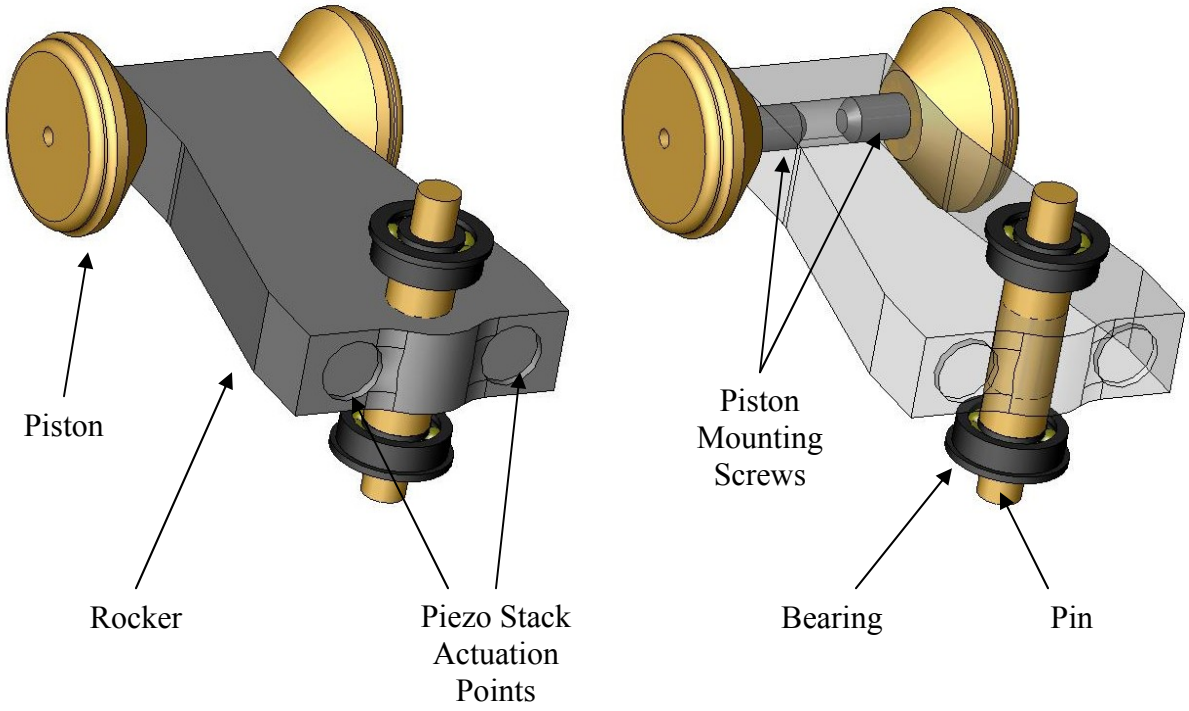

Figure 5.1.6: CAD model of the mechanical amplifier

5.1.3 Hydraulic Amplifier

The hydraulic amplifier consists of pistons, belloframs, bellofram retainers, and hydraulic actuator. A detailed partial section view of the hydraulic amplifier is shown in Figure 5.1.6.

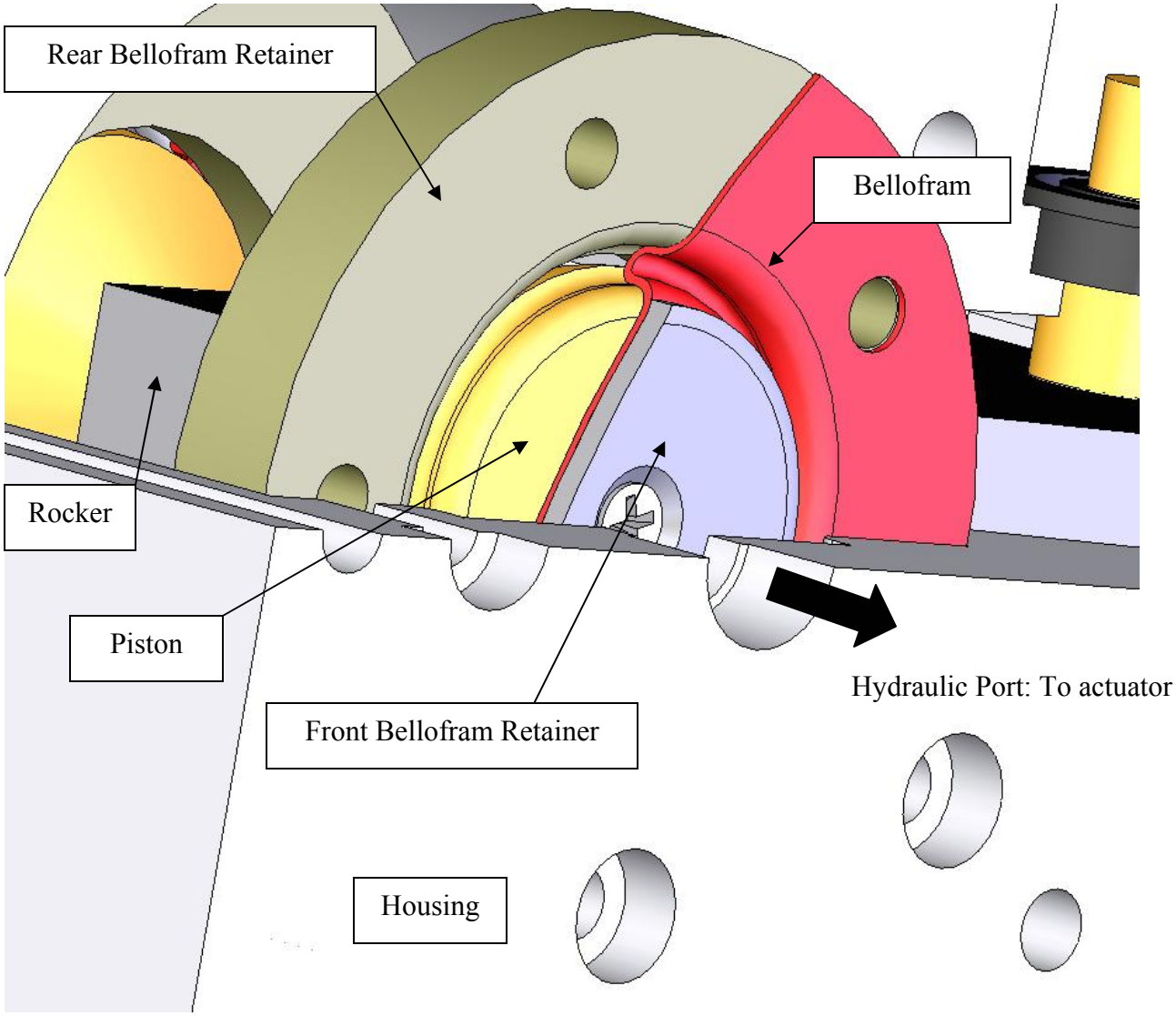

Figure 5.1.6: Detailed partial section view of the hydraulic amplifier

As shown in the figure the outer section of the bellofram is restrained between the rear bellofram retainer and the housing. The inner section of the bellofram is sandwiched between the front retainer and the piston using a 4-40 countersunk screw. This allows the inner section to displace with respect to the outer section, while maintaining the shape of the bellofram and a fluid seal. The edges of the piston and rear retainer are sculpted to tightly backup the bellofram in order to minimize system compliance associated with ballooning of the bellofram. The fluid volume is

minimized in order to decrease the amount of system compliance introduced by the fluid compressibility.

To remove all entrapped air in the fluid, a method to bleed the system must be incorporated in the design. Fluid for both sides of the hydraulic amplifier is stored in a common reservoir under pressure, which can be separated from the system. During the bleeding process, fluid from the reservoir passes out a common line to a tee, where to branches out to both sides of the hydraulic actuator, shown in Figure 5.1.7. Both hydraulic lines incorporate a ball valve between the tee and the hydraulic actuator, so the fluid flow can be stopped and the actuator assembly can be removed from the fluid reservoir for testing.

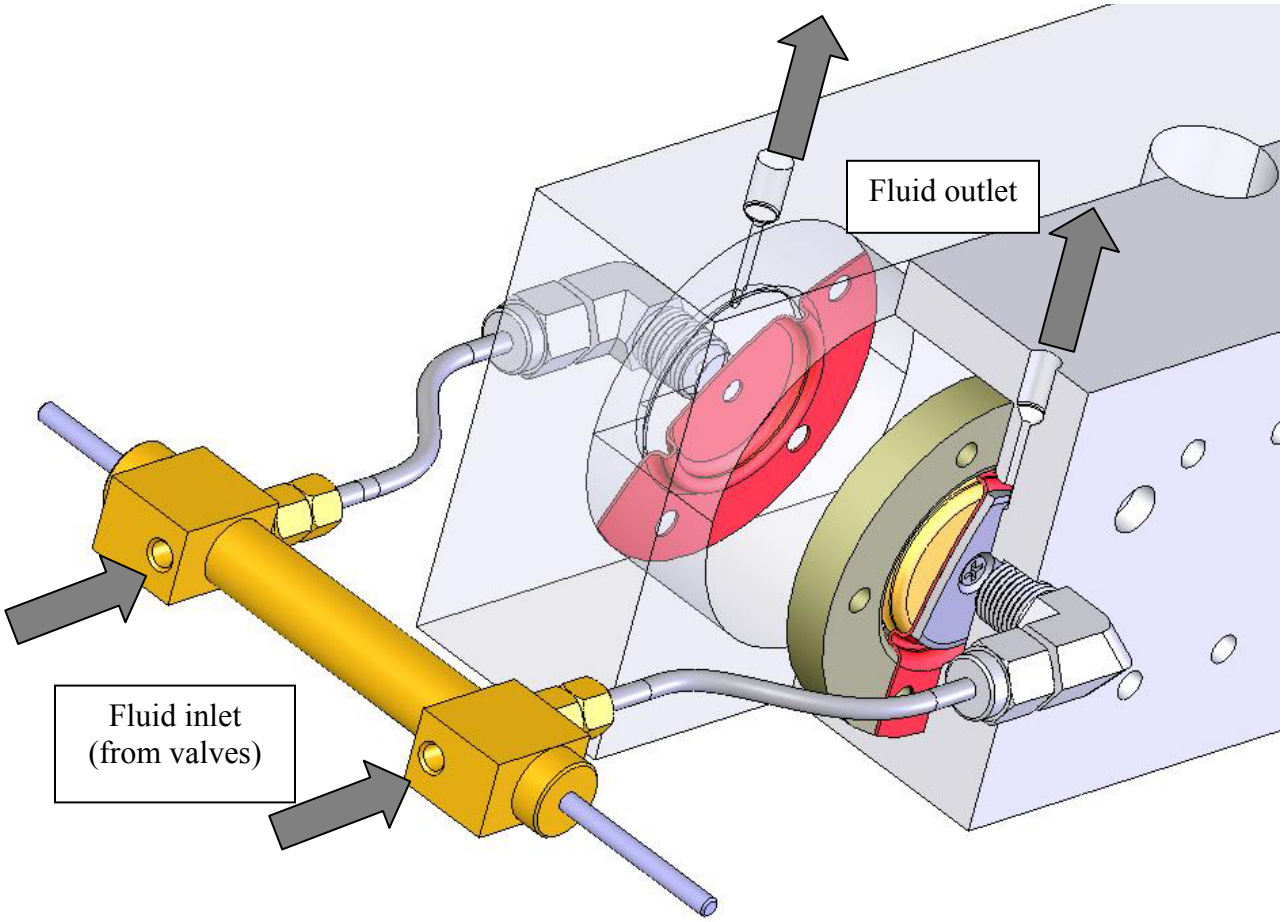

Figure 5.1.7: Hydraulic bleeding schematic

The fluid flows from the hydraulic actuator to the fluid chambers, formed by the housing and the belloframs, through two small lengths of 1/8" diameter stainless steel tubing. Fluid exits the chambers through a port at the highest point. The port uses an automotive brake bleed screw so that fluid flow can be stopped. Having the port at the highest point allows all the air entrapped in the system to flow out the port as fluid is introduced into the system from the reservoir.

5.1.4 Single Crystal Modification

The original design was created with the intent of substituting single crystal piezoelectric stacks for the EPCOS PZT stacks. Since the single crystal stacks produce more displacement output per unit length, shorter single crystal stacks are needed to achieve the same system displacement. Alumina spacers were included to occupy the difference in space required by the two types of stacks. Figure 5.1.8 depicts how the existing design is retrofitted with single crystal stacks.

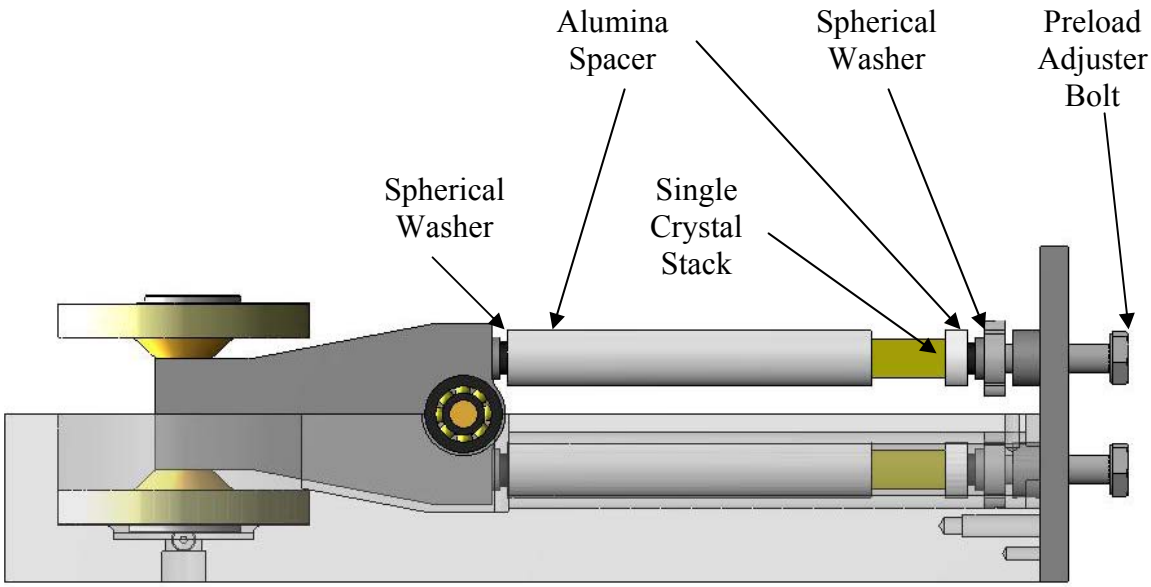

Figure 5.1.8: Actuator assembly with single crystal stacks

5.2 Finite Element Analysis

Finite-Element Analysis (FEA) was performed on critical system components to ensure that they were of adequate strength and their deflections under typical system loads were much less than the output of the piezoelectric stacks. The components analyzed were the rocker, pin, and end cap. Analysis was performed using the software package COSMOS. COSMOS was fully integrated into the CAD package, enabling rapid analysis of small design changes. The results for each component analyzed are discussed in the following subsections.

5.2.1 Finite Element Analysis of the Rocker

The rocker was determined to be a critical component in terms of both stress and deflection, since it is directly acted upon by the piezoelectric stacks. Components in direct contact with the stacks will be subjected to the largest forces and the smallest displacements, since the stacks displacement has not yet been amplified and the force has not been attenuated.

The rocker was subjected to a variety of boundary conditions and as a result of the analysis, the component underwent three revisions.

The forces acting on the rocker are applied by the stacks and by the hydraulic pistons when the system is working against a load. In order to ensure the piezoelectric stacks will remain in compression during the device operation, a preload of 5 MPa was applied to both stacks. The blocked stress produced by the stack was estimated as 25 MPa. The forces applied to the rocker can be calculated from the stresses using the cross sectional area of the piezo stacks. The dimensions of the piezoelectric portion of an EPCOS stack were measured to be 6.48 mm by 6.48mm. The stack measured was from a previous order and it dimensions differed slightly from the stacks used in testing, whose dimensions were 6.80mm by 6.80mm. Using the cross sectional area measured, the preload force was 210 N and the blocked force was 1050 N. The critical loading condition occurs when the rocker is not allowed to rotate about the pivot while one stack is actuated by the full electric field and the other stack is only experiencing the preload force. The force applied at the output of the rocker needed to balance the moment produced by the stacks at this loading condition is 168 N. This balancing force is calculated using the rockers amplification ratio, which is five. The object of the finite element analysis was to ensure under maximum load, the rocker tip deflections would be less than 6.35μm (0.00025" or .25 mils).

The first loading condition examined was the input of the rocker was not allowed to rotate or translate while a force of 168 N was applied to the rocker output. The results from the stress and displacement analysis are shown in Figures 5.2.1 and 5.2.2 respectively.

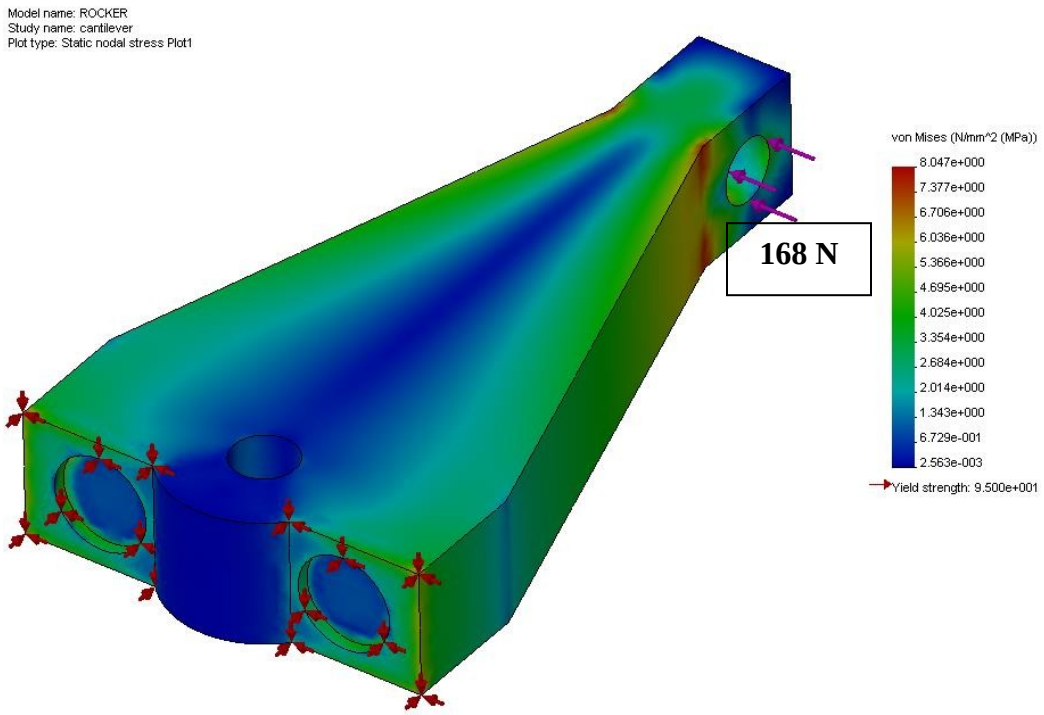

Figure 5.2.1: Von Mises stress for cantilevered rocker (MPa)

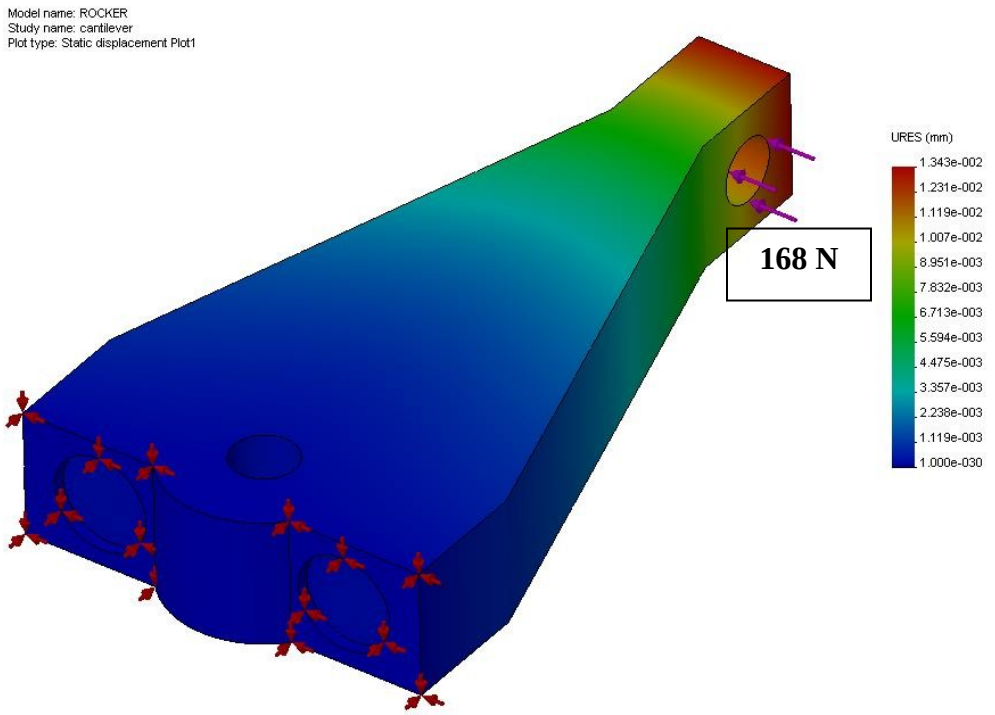

Figure 5.2.2: Resulting displacement for cantilevered rocker (mm)

The boundary conditions used in this analysis do not accurately represent what the rocker would experience under normal operating conditions, but make it convenient to compare the results of the finite element analysis to calculations performed using beam deflection theory.

Beam deflection calculations were performed on a cantilevered bar of identical dimensions to the tip of the rocker to ensure the accuracy of the finite element analysis. The dimensions of the beam are shown in Figure 5.2.3.

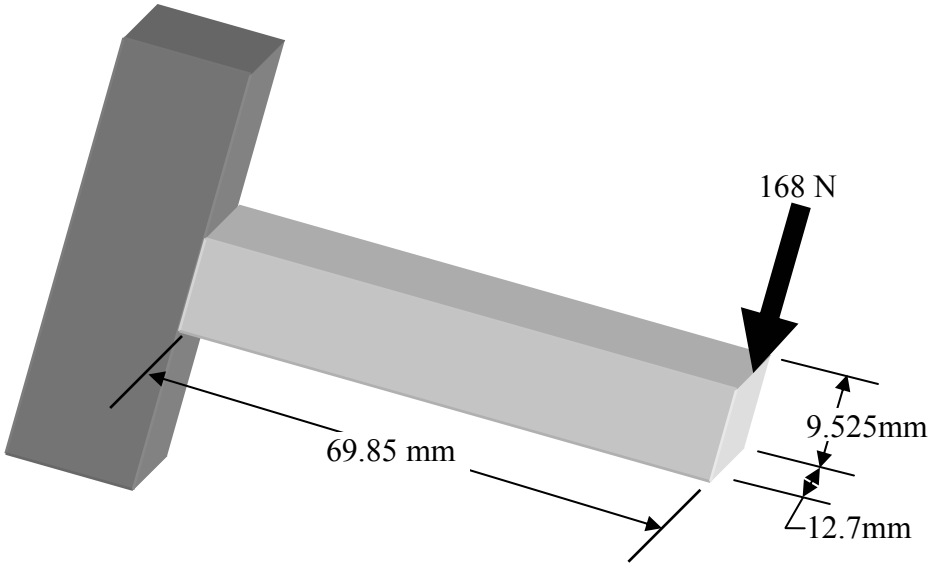

Figure 5.2.3: Beam dimensions

The deflection at the end of the beam is given by Equation(5.2.1).

$$\Delta = \frac{PL^3}{3EI} \tag{5.2.1}$$

Using the elastic modulus of 7075 aluminum, 71.1 GPa, the deflection at the end of the beam is 0.293mm (0.0116”) which is larger that the results obtained from the FEA, which was 0.013mm (0.0005”). This result represents a worst case scenario, in actually the deflection in the rocker will be must smaller due its moment of inertia being larger that that of the beam analyzed.

The boundary conditions for the FEA were changed to more accurately represent what the rocker would experience under normal operation. A force of 168 N was applied at the output of the rocker as in the previous analysis. Forces of the 1050 N and 210 N were applied at the stack actuation points such that the resulting moment about the pin is zero. The pin translation was restrained, but was allowed to rotate. The stress and displacement results are show in Figures 5.2.4 and 5.2.5 respectively.

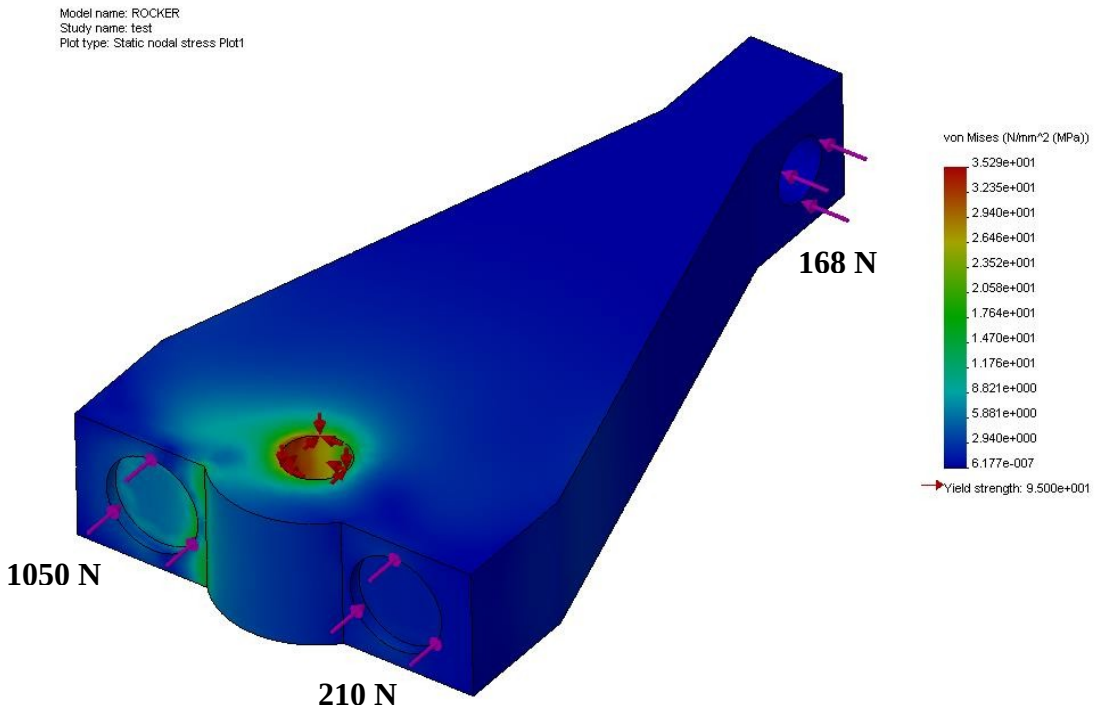

Figure 5.2.4: Von Mises stress for initial rocker design, restrained about the pin hole (MPa)

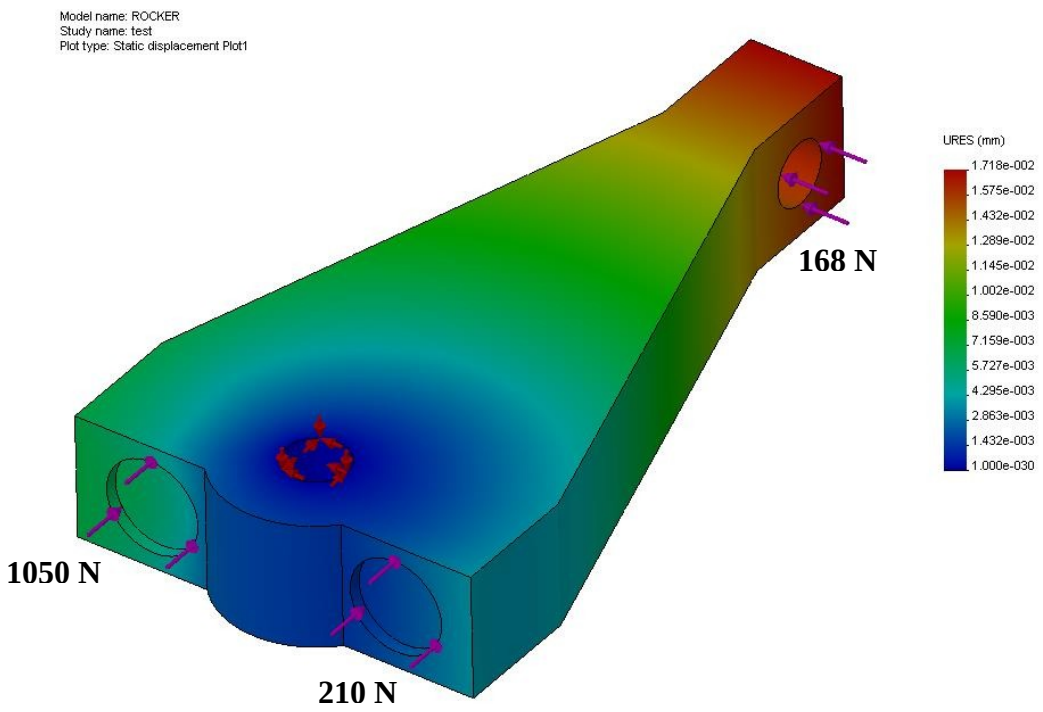

Figure 5.2.5: Deflection for initial rocker design, restrained about the pin hole (mm)

Although the stresses in the rocker do not exceed the yield stress for 7075 aluminum, the deflections under load, 17.13µm ($0.6x10^{-3}$in) exceeds the maximum deflection criterion imposed on the rocker of 6.35µm ($0.25x10^{-3}$in). To increase the rocker stiffness, the width dimension was increased from 9.53mm 16.51mm (0.375in to 0.650in). The finite element analysis was repeated on the redesigned rocker and the stress results are shown in Figure 5.2.6 and the deflection results are shown in Figure 5.2.7.

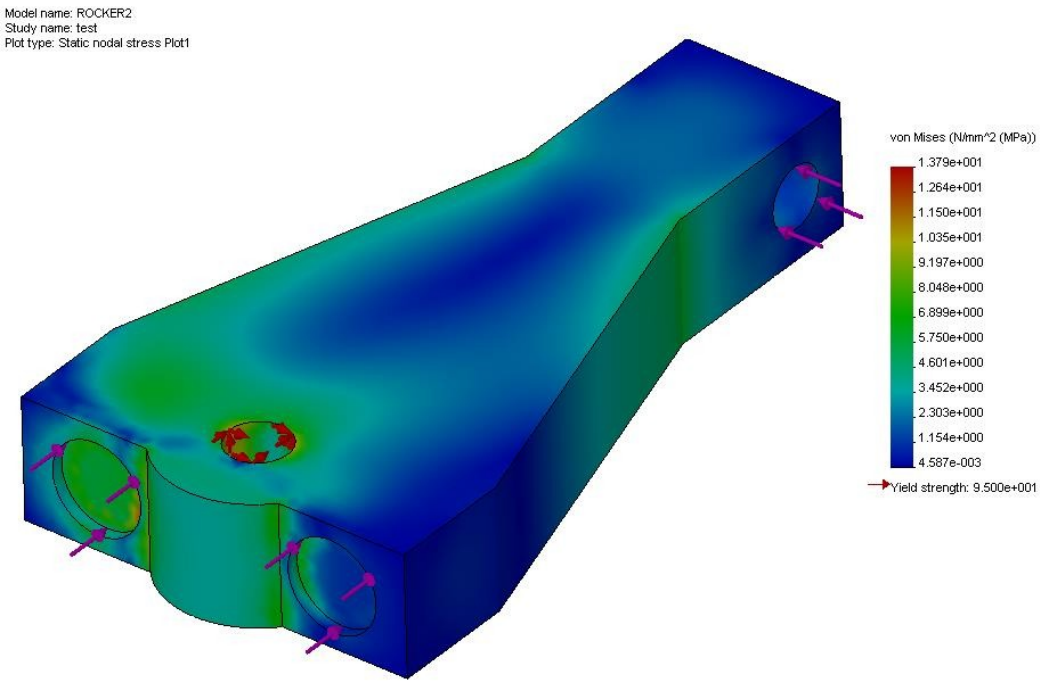

Figure 5.2.6: Stress results for resigned rocker (MPa)

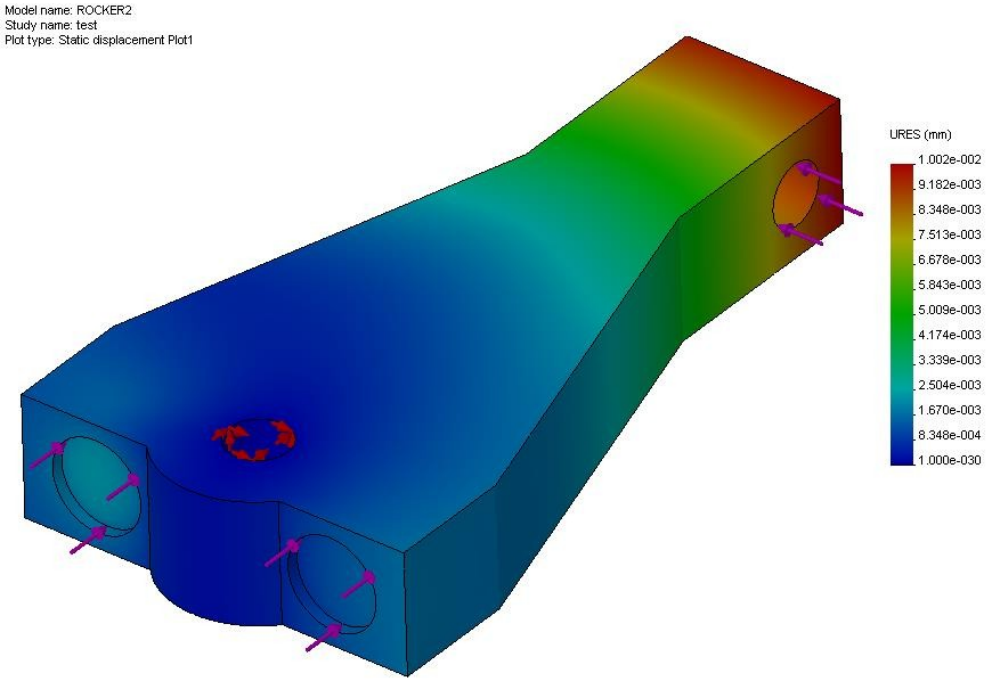

Figure 5.2.7: Deflection results for redesigned rocker (mm)

The redesign of the rocker decreased the deflection under maximum load to 10.02μm ($0.394x10^{-3}$in), but the redesigned rocker still did not pass the maximum permitted deflection. The rocker was redesigned for a second time increasing the width at the tip of the rocker to 25.4mm (1.000in). The stress and displacement results are shown in Figures 5.2.8 and 5.2.9 respectively.

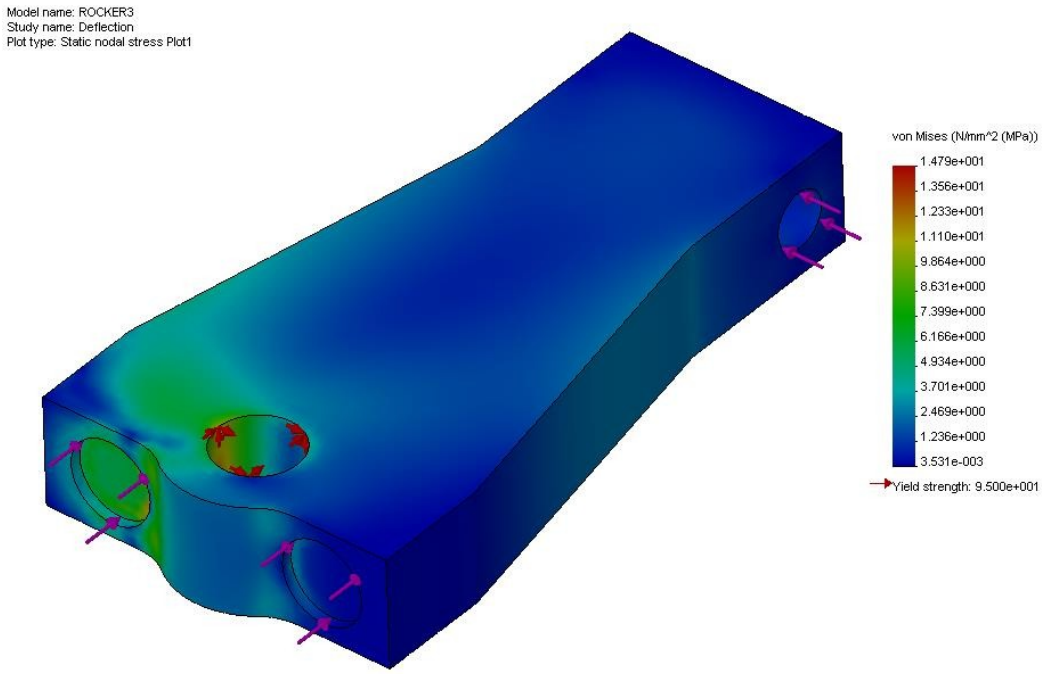

Figure 5.2.8: Stress results for second rocker revision (MPa)

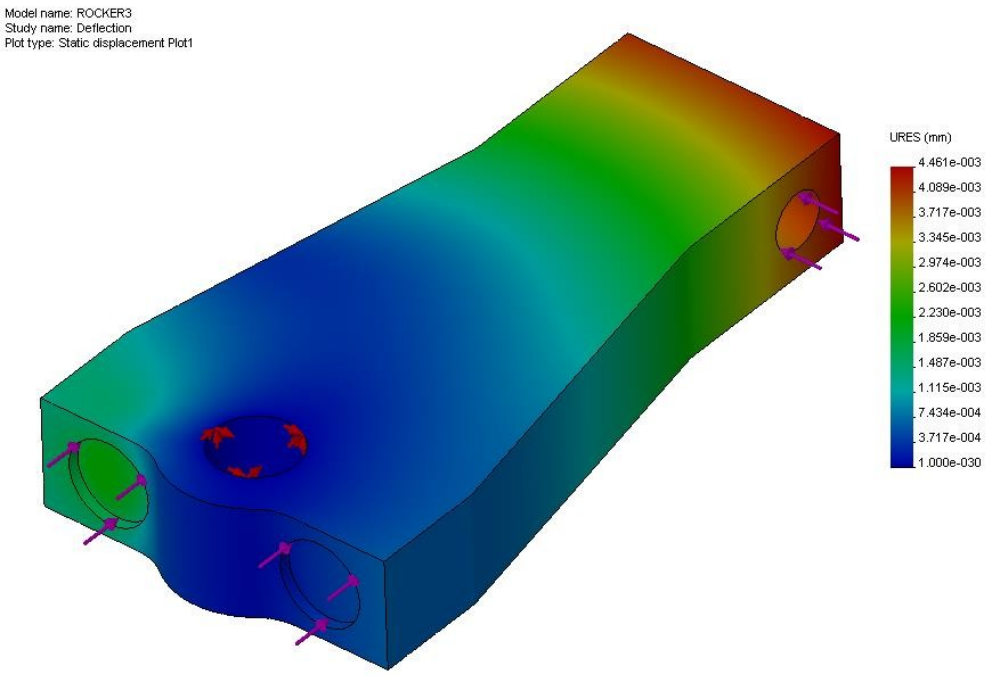

Figure 5.2.9: Deflection results for second rocker revision (mm)

The third iteration of the rocker deflects 4.46µm ($0.176x10^{-3}$in) under full load, which is less than the maximum permitted deflection of 6.35µm ($0.250x10^{-3}$in). Now that the rocker is of sufficient strength and stiffness the pin that the rocker rotates about can be analyzed.

5.2.2 Finite Element Analysis of the Pin

Finite element analysis was performed on the pin. Figure 5.2.10 shows the areas on the rocker where forces and restraints are applied.

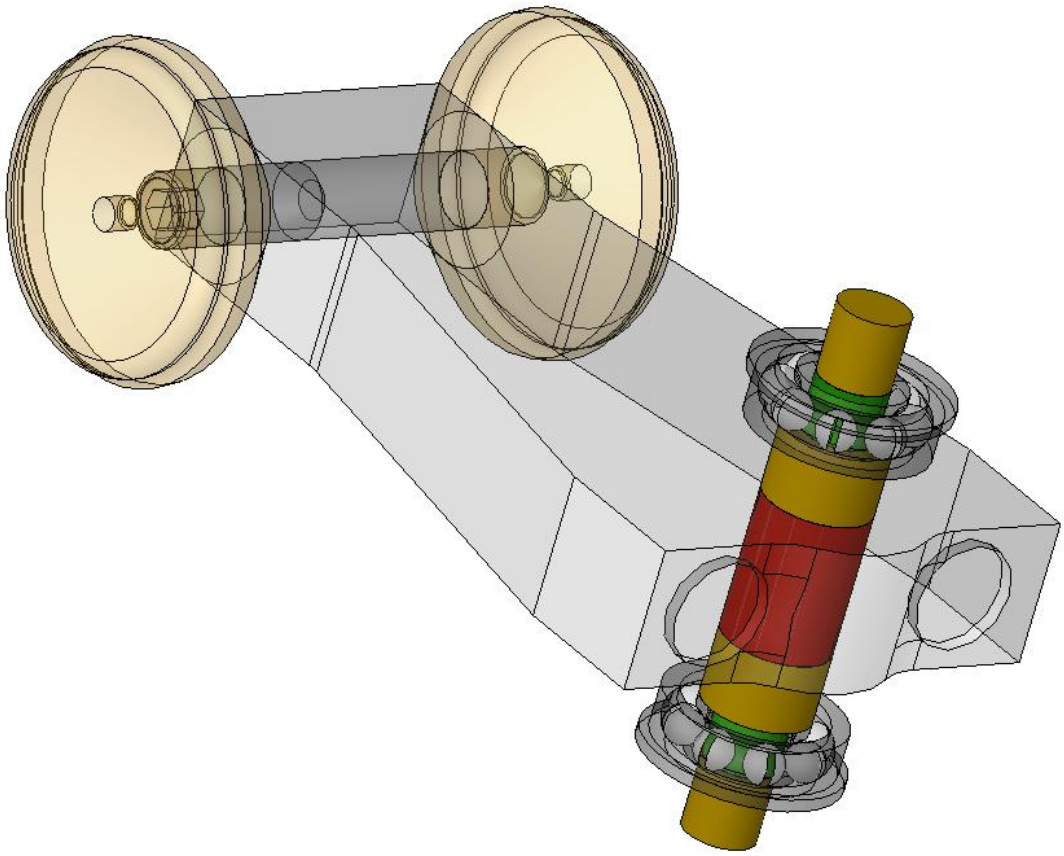

Figure 5.2.10: Pin action (red) and restraint points (green)

Forces experienced by the rocker are transmitted through the pin to the housing, shown in red in previous figure. The restraints are applied at the interface between the bearings and the pin, shown in green. The pin was examined under a number of loading conditions to determine stresses and deflections.

The first loading condition examined is effect of the stack preload forces on the pin. The sum of the preload forces for both stacks is 420N (94.4lb). Figures 5.2.11 and 5.2.12 show the stress and displacement results from the finite element analysis of the pin under preload forces.

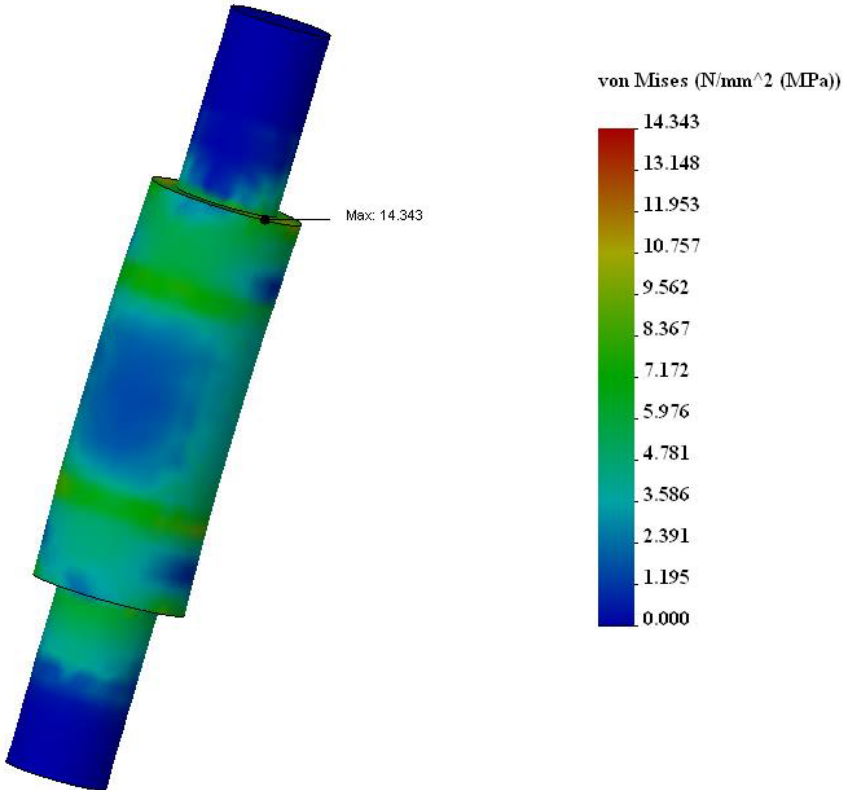

Figure 5.2.11: Von Mises stress results for pin under preload forces only (MPa)

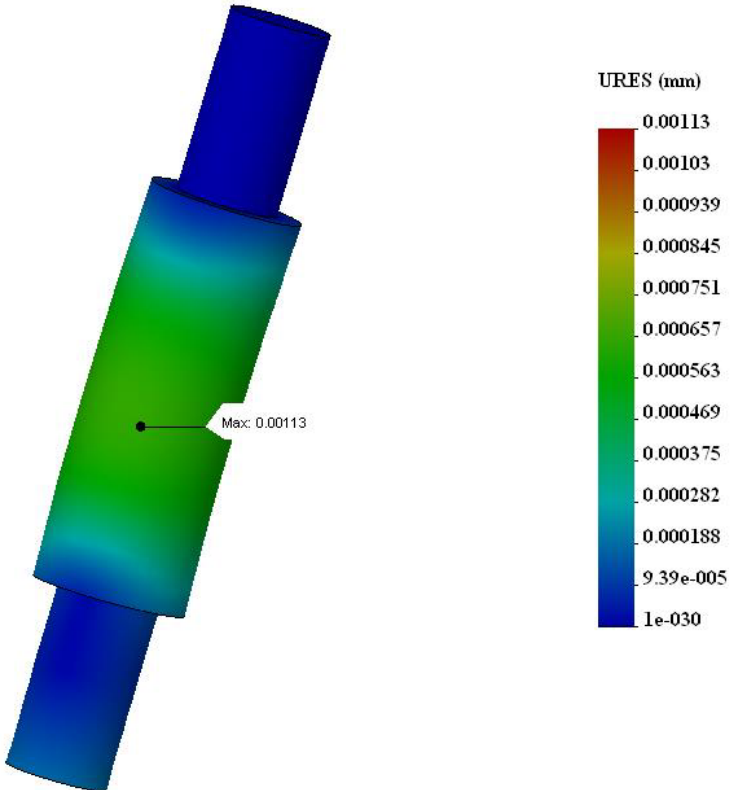

Figure 5.2.12: Deflection results for pin under preload forces only (mm)

The stack preload forces produce a maximum bending stress in the pin of 14.3 MPa and a maximum deflection of 0.00113mm.

The second loading condition investigated was the effects of the preload and blocked forces acting on the pin. Each stack will produce a force of 1050 N at a stress level of 25 MPa, which equates to a total force acting on the pin of 2100 N. Figures 5.2.13 and 5.2.14 show the stress and displacement results from the finite element analysis of the pin under preload and blocked forces.

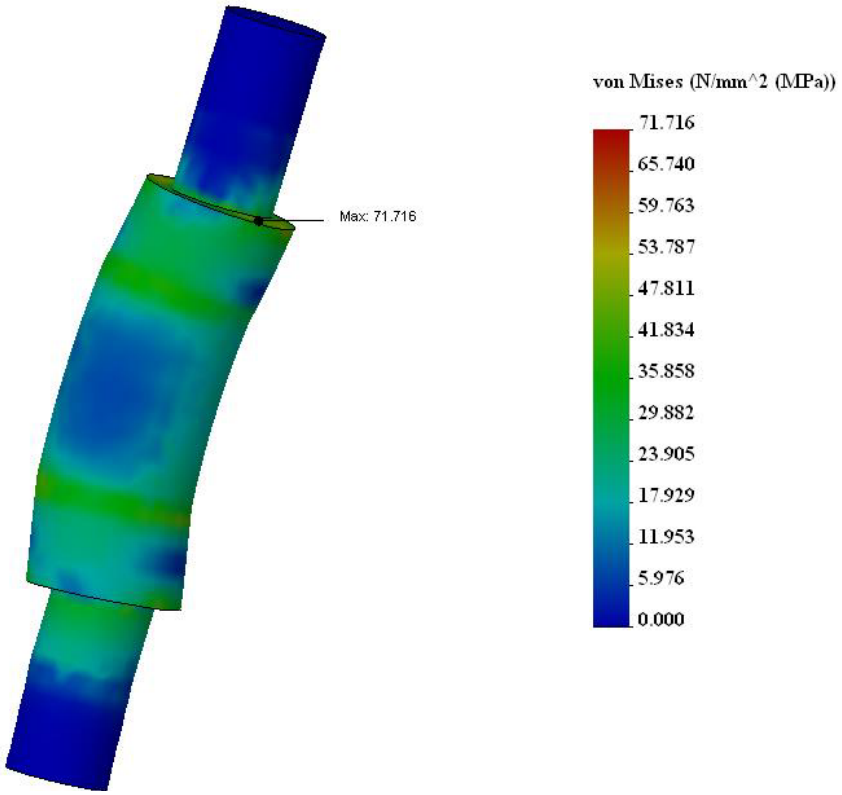

Figure 5.2.13: Von Mises stress results for pin under preload and actuation forces (MPa)

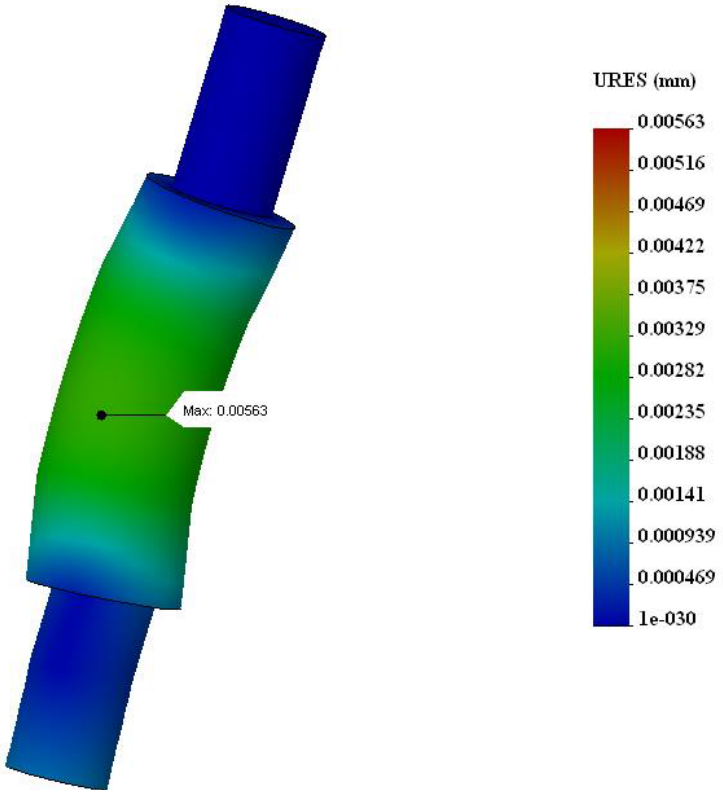

Figure 5.2.14: Deflection results for pin under preload and actuation forces (mm)

Subtracting the deflection under preload (0.00113mm) from the deflection produced by the stack forces (0.00563mm), the working deflection can be determined. The working defection is 0.0045mm ($0.177x10^{-3}$in) based on the previous finite element results.

5.2.3 Finite Element Analysis of the End Cap

The final component analyzed using finite element analysis is the end cap, which must resist the stack forces under preload and actuation. Figure 5.2.15 shows the applied loads and restraints on the end cap.

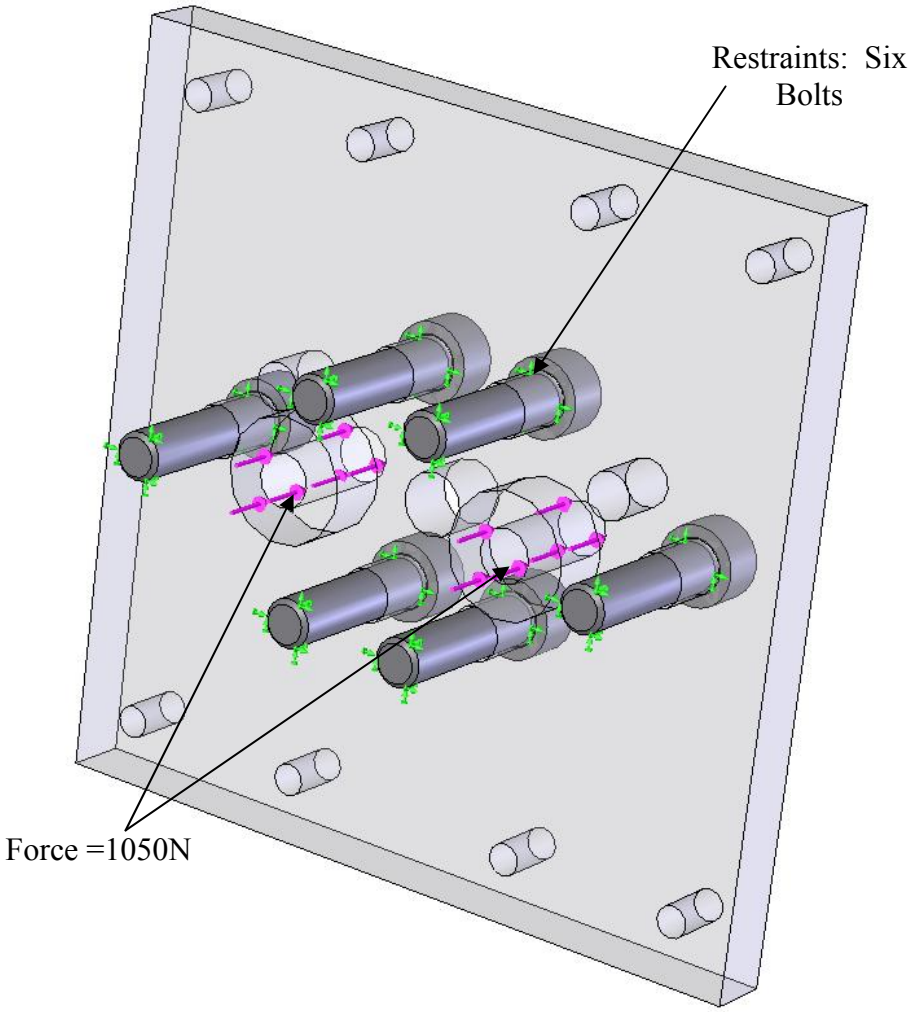

Figure 5.2.15: Forces (pink) and restraints (green) for FEA of end cap

Actuation and preload forces totaling 1050 N were applied in the threaded hole for the preload adjuster. The forces represent a worst case scenario, if both stacks were actuated at the same time. In reality the stacks will operate out of phase, so the forces experienced by the end cap will be less than used in this analysis. The end cap was restrained by fixing the displacements of the shanks of the six bolts used to attach the end cap to the left and right housings. The interface between the bolt heads and end cap were modeled as if they were bonded together, meaning no relative displacement were permitted between the parts.

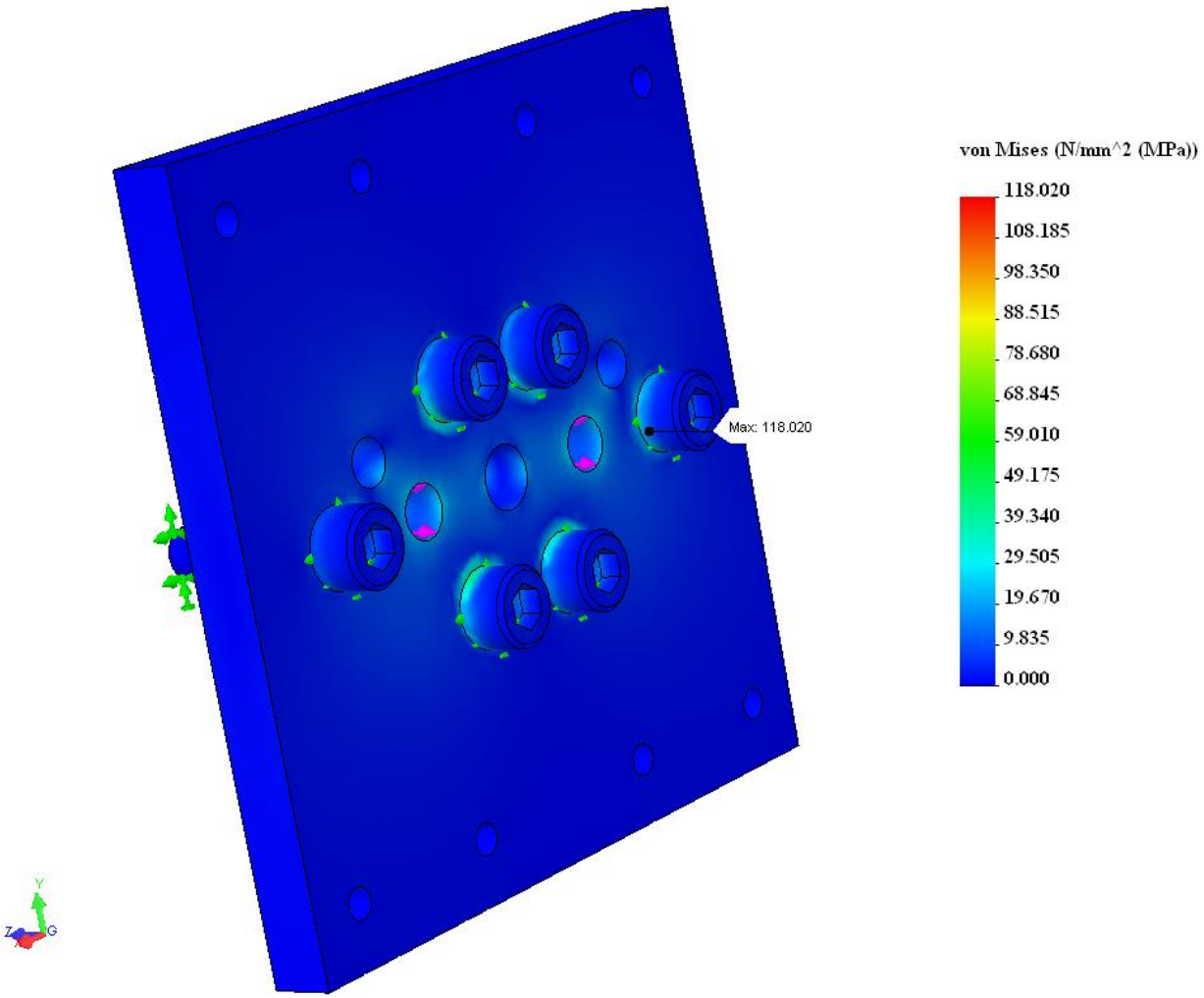

Figure 5.2.16: End cap stresses under stack actuation forces (MPa)

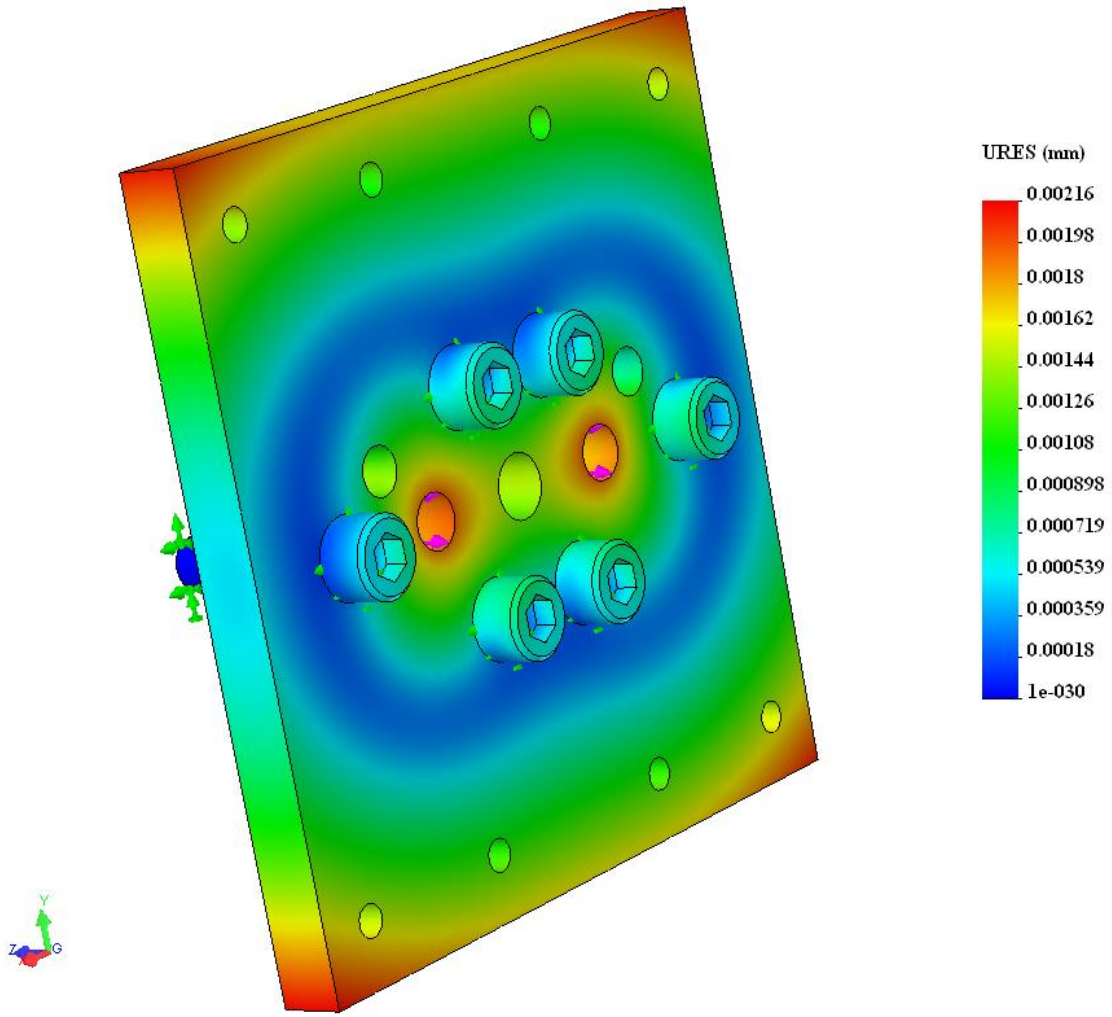

Figure 5.2.17: End cap deflections under stack actuation forces (mm)

Using the probe tool in COSMOS, the maximum deflection in the threaded holes for the preload adjuster is 0.00178mm (7.01×10^{-5}in). This deflection is two orders of magnitude below the stack displacement; end cap deflections will not hinder system performance.

5.2.4 Finite Element Analysis Summary

Finite element analysis determined that the critical components of the design were adequate to resist the stresses imposed on them by the piezoelectric stacks. The component deflections under load proved to be the limiting factor in the component design. The deflection

results for the rocker showed that a design modification was required to increase its stiffness. The pin and end cap were shown to have adequate stiffness and required no modifications. The use of finite element does not account for residual stress present in the components after machining. Thus sufficient factors of safety are used to ensure that failures do not occur during operation. Overall finite element analysis proved to be a useful tool to ensure maximum device performance by elimination of elastic compliances.

CHAPTER 6: EXPERIMENTAL TESTING AND RESULTS

6.1 Assembly

Prior to testing the actuator system was assembled. The assembly process included making the necessary tubing segments to connect the actuator assembly and the external hydraulic cylinder. Also a system to fill and purge any entrapped air from the hydraulic system was developed.

The bleeding system consisted of a pressurized hydraulic reservoir, several valves and the necessary tubing. A schematic of the system is shown in Figure 6.1.1.

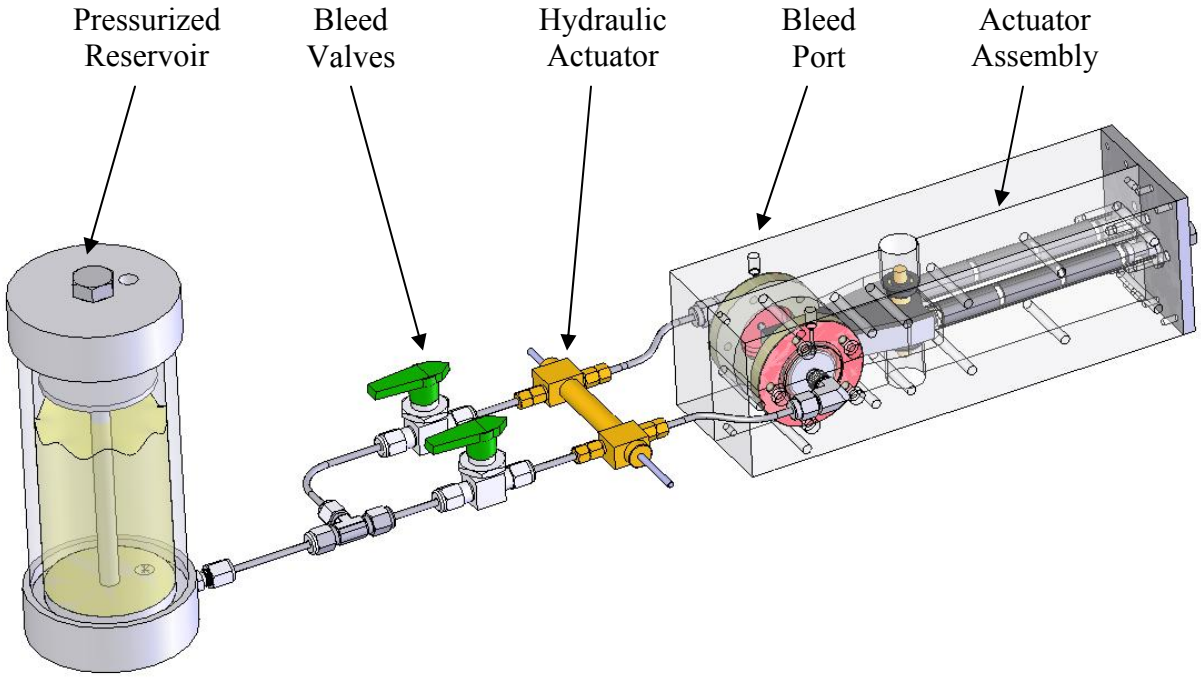

Figure 6.1.1: Hydraulic system bleeding schematic

The hydraulic oil, which is Dow Corning 200 fluid, is stored in the reservoir under air pressure applied through the port on the top of the reservoir. The air pressure came from two sources depending on the pressure desired. For low pressure, less than 862 kPa (125psi), compressed air from an air compressor was used to pressurize the reservoir. If higher pressures were desired, compressed nitrogen from an air cylinder was regulated to achieve the sought pressure.

The bleeding procedure consists of circulating fluid from the pressurized reservoir through the open bleed valves, the hydraulic actuator, and into the hydraulic segment of the actuator assembly. Fluid escaped the actuator assembly through bleed ports at the highest point, which were fitted with automotive brake bleed screws. To aid the extraction of air from the system, the hydraulic actuator was cycled back and forth by hand while the fluid was flowing through it.

Following the bleeding procedure, the bleed screws on the actuator assembly are closed first. This allows the fluid in the system to reach the pressure applied to the reservoir. The bleed valves are then closed, trapping the pressurized fluid in the system for testing. Having the fluid in the system under pressure will help system performance. The pressure will preload the seals in the hydraulic system, minimizing their deflection during system operation. Any remaining air bubble will be reduced in size by the pressure, which will minimize the fluid compliance. Following the bleeding procedure, the pressurized reservoir can be removed and the system is ready for testing.

6.2 Experimental Setup

The schematic of the experimental setup is shown in Figure 6.1. The experimental setup will be discussed in detail in the subsequent paragraphs.

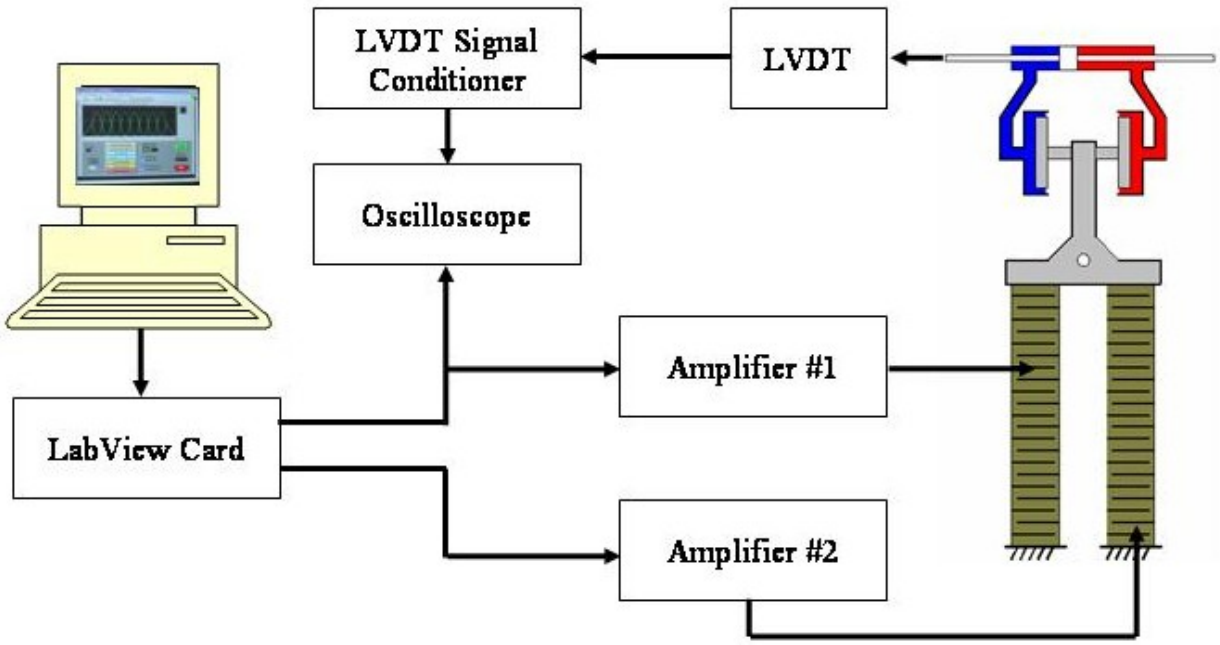

Figure 6.2.1: Schematic of Experimental Setup

The piezoelectric stacks on each side of the rocker were driven with a separate amplifier. The amplifiers used were Kepco model BHK 1000-0.2MG, which are capable of providing 1000V and 200 mA and use an amplification ratio of 100 times. The input signals for the amplifiers were created in the PC using LabView software and were output to a digital-to-analog converter on the LabView card connected to the PC. Separate signals for each amplifier were generated, since the stacks are driven out of phase. The drive signal used for each amplifier was a sine wave ranging from 0 – 1.6V, with varying frequency. The amplifiers produced and output of 0 – 160V in response to this input. Figure 6.2.2 shows a screen shot of the LabView program used to generate the drive signals.

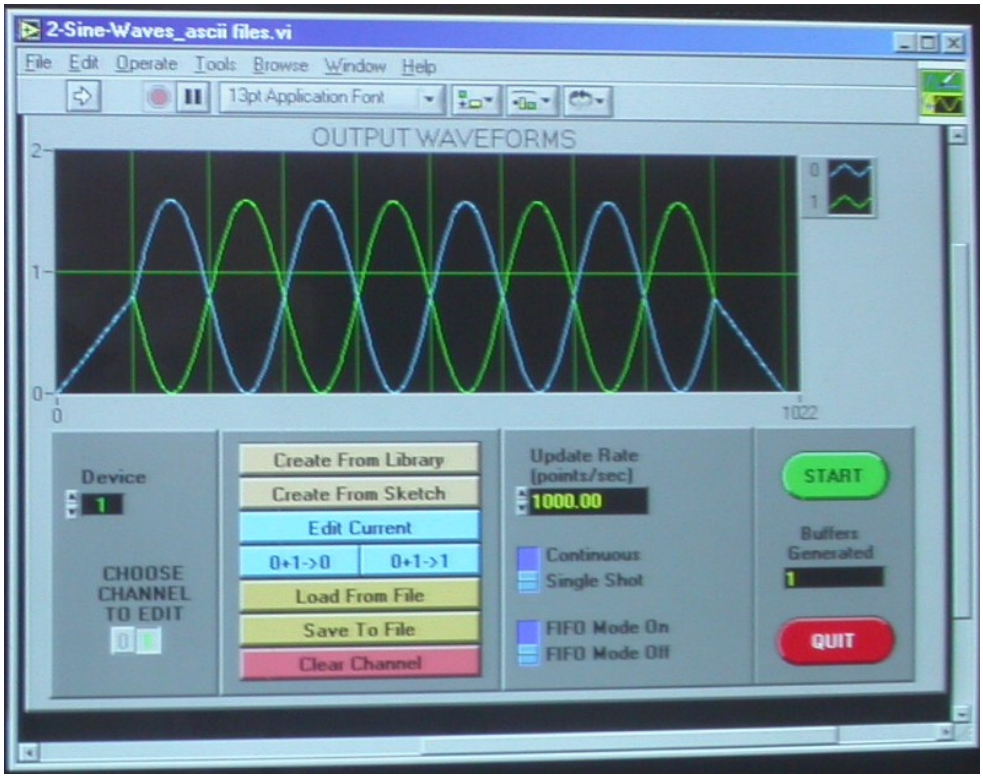

Figure 6.2.2: Screen shot of LabView signal generation interface

Notice in Figure 6.2.2 how the signals (shown in green and blue) initially ramp up and ramp down together at startup and shutdown respectively. The reason for this is to minimize the possibility of damaging the stacks with a large step voltage input. In between startup and shutdown the voltages of the two stacks are the out of phase sine wave described earlier.

A test stand was fabricated so that the systems force and displacement can be characterized as a function of frequency. The test stand consists of an aluminum plate with fixtures to hold the hydraulic actuator and devices to measure displacement and force. Displacement was measured by a Schaevitz linear variable displacement transducer (LVDT) model 500-MHR connected to a Schaevitz model ATA 2001 LVDT signal conditioner. The output of the LVDT signal conditioner was read on an oscilloscope. The sensitivity of the LVDT system was determined to be 17.42μm (0.686 $x10^{-3}$ in) and was able to measure oscillatory displacements at frequencies up 1000 Hz. The force produced by the device was

measured by allowing the device to actuate against a known force. The known force was applied via a mass suspended by a string, which is attached to the hydraulic actuator. The device operates against the gravitational force applied by the mass. Figure 6.2.3 shows a schematic of the test stand.

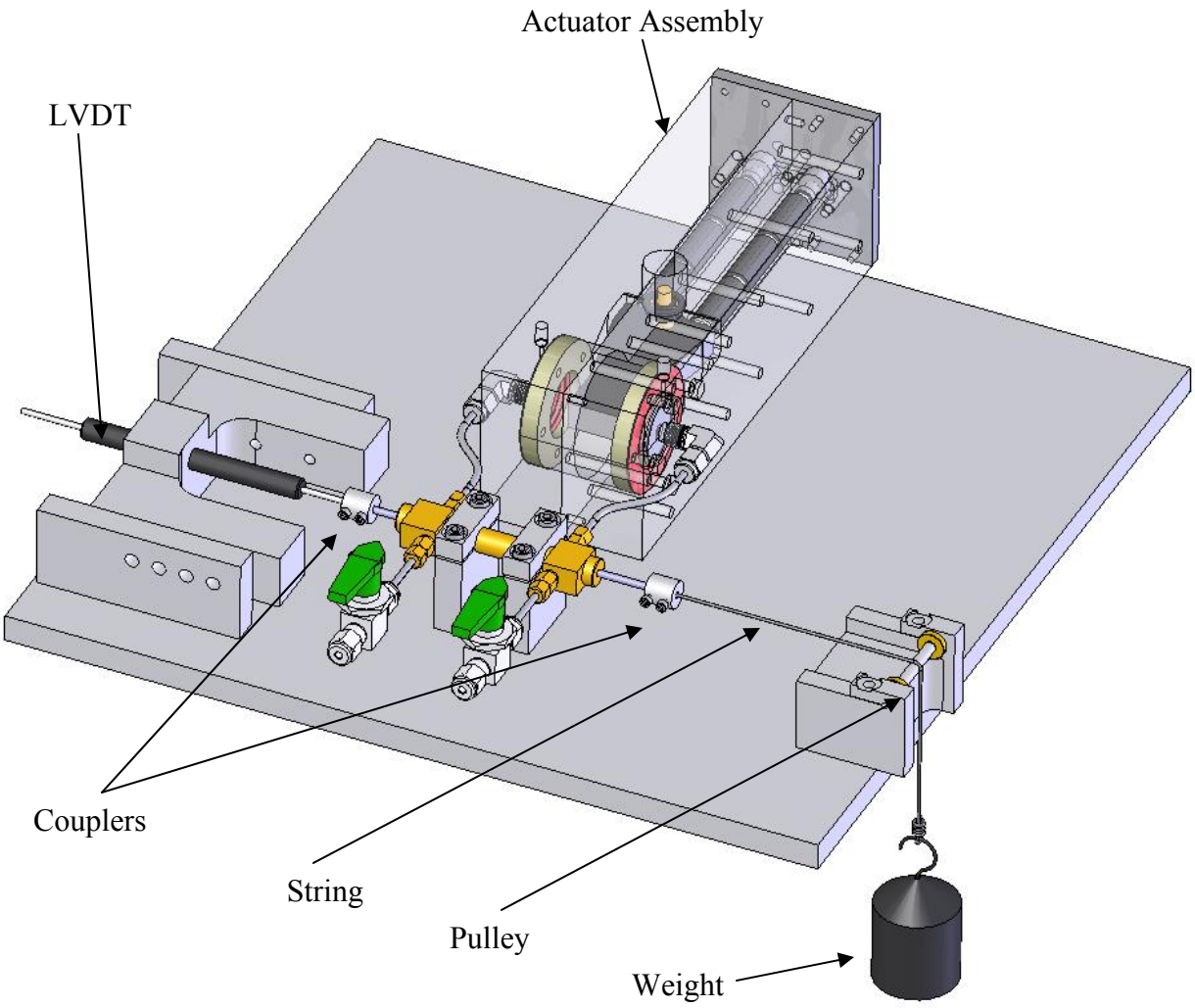

Figure 6.2.3: Test stand schematic

The string attaching the mass and the hydraulic actuator was draped over a pulley to convert the horizontal motion of the actuator to vertical motion in the mass. A consequence of the large

displacement amplification of the piezoelectric stacks is there is a large force amplification when forces are applied to the hydraulic actuator. Meaning the piezoelectric stack will experience a large force, when a small force is applied to the hydraulic actuator. It is possible to induce a ferroelastic switch in the piezoelectric stacks by applying a large compressive force. For this reason the force applied to the actuator will be limited to 22.24 N (5lb).

6.3 Displacement Testing

The actuators displacement was characterized as a function of frequency. Tests were conducted under various fluid bias pressures and applied voltages. Figure 6.3.1 shows a plot of device displacement versus drive frequency for 160 V_{pp}.

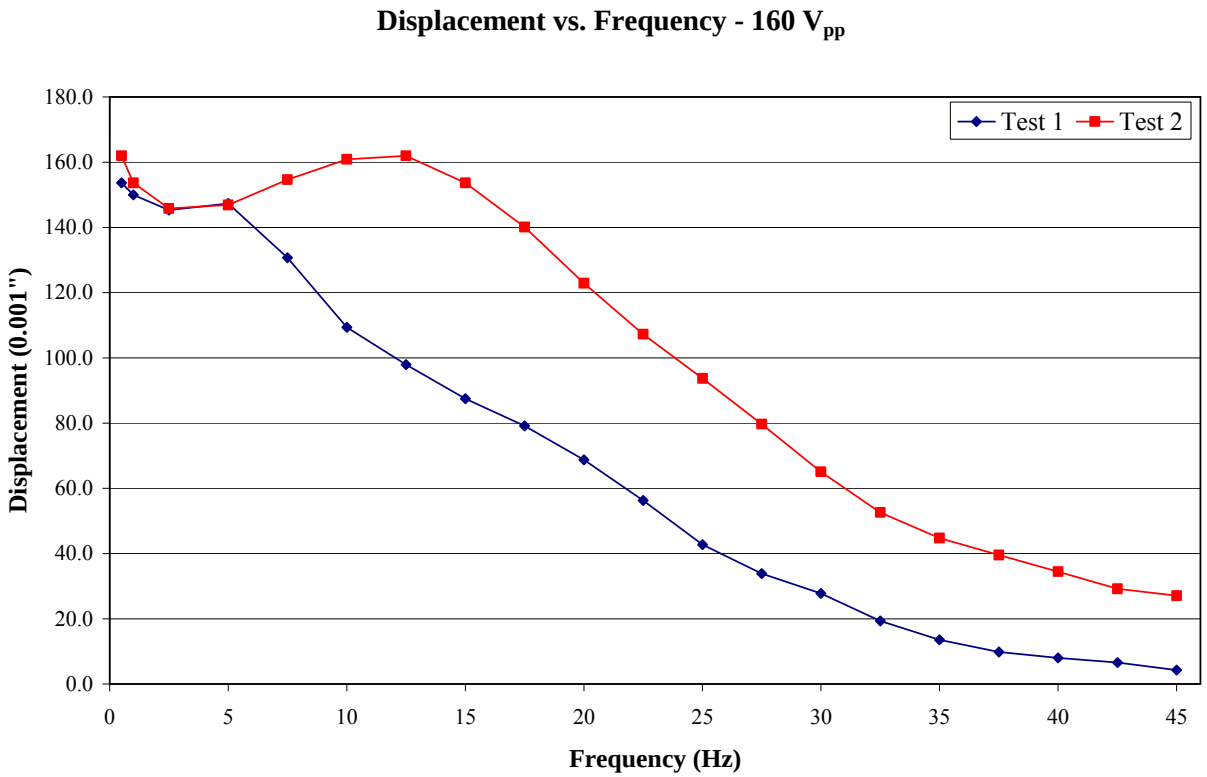

Figure 6.3.1: Displacement results for tests using 160V_{pp} drive voltages

The results shown in Figure 6.3.1 show the averaged results of three trials for two sets of displacement tests. Test 1 was conducted using a bias pressure of 344.7kPa (50psi). The system was re-bled and test 2 was conducted using a bias pressure of 517.1kPa (75psi). The discrepancies between test results can be attributed to air trapped in the hydraulic system. Test 2 is believed to be representative of the true system performance. Figure 6.3.2 shows displacement results for test two with error bands calculated for a 95 percent confidence interval.

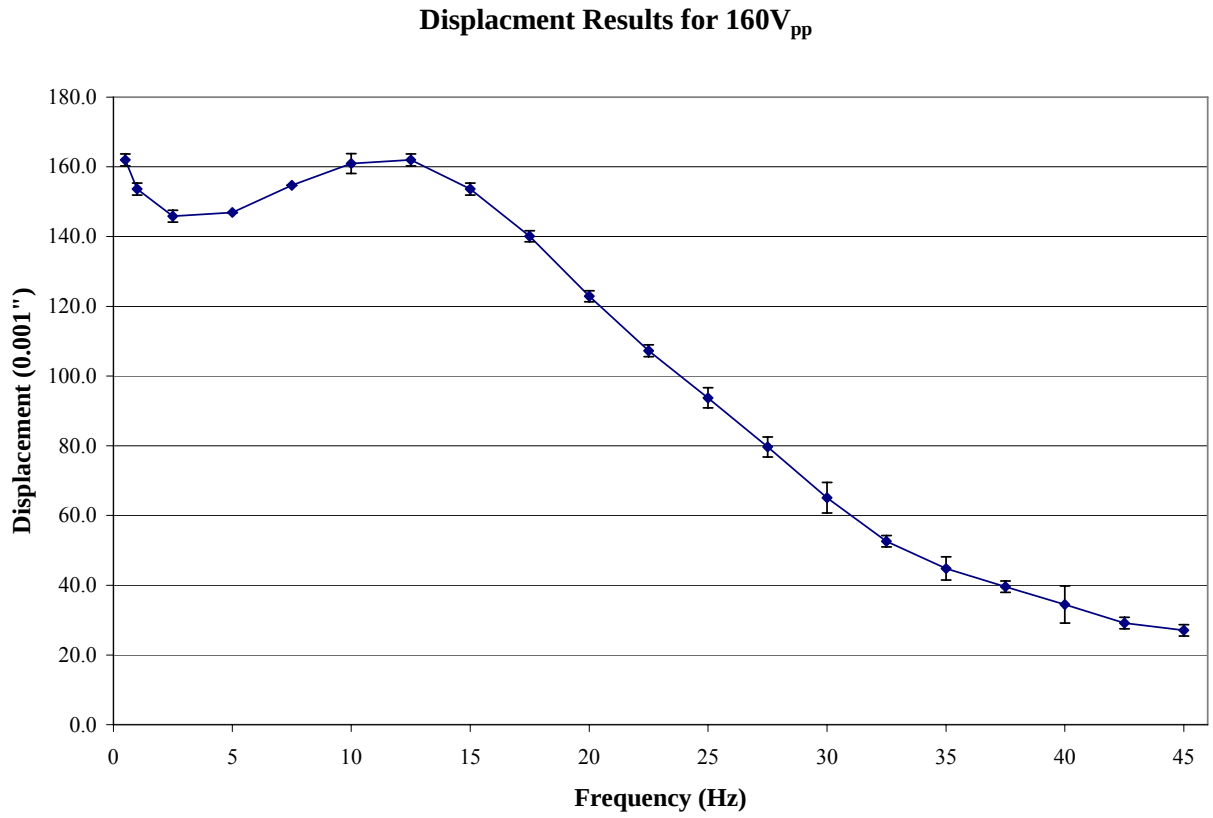

Figure 6.3.2: Displacement results for test using $160V_{pp}$ drive voltages with error bars

The confidence interval was calculated using the t-distribution and the formula for a small sample size given in Equation(6.3.1).

$$\bar{x} \pm t_{\alpha/2} \frac{s}{\sqrt{n}} \tag{6.3.1}$$

$\bar{x}$ is the mean, s is the standard deviation, n is the number of samples, and $t_{\alpha/2}$ is the values from the t-distribution using 95% confidence interval and 3 degrees of freedom.

The large falloff in performance after 15 Hz is attributed to the 200 mA current limitation of the power supply used. To theoretically validate the current limit, the electrical subsystem can be modeled as a sinusoidal voltage source driving a capacitor, since a piezo act as capacitors. A schematic of the electrical system is show in Figure 6.3.3.

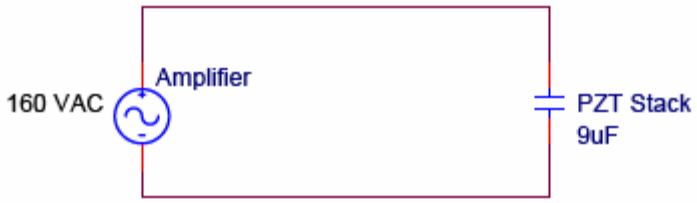

Figure 6.3.3: Electrical Schematic

The theoretical current limit can be obtained using Equations (6.3.2) – (6.3.8):

$$V = \frac{Q}{C} \Rightarrow Q = V \cdot C \tag{6.3.2}$$

Where Q is charge, C is capacitance and V is the time dependent voltage given by Equation(6.3.3).

$$V(t) = V_{\max} \cdot \sin(\omega t) \tag{6.3.3}$$

V_{max} is the amplitude of the signal, which is 160 V, and ω is the frequency in radians/second. Substituting this back into equation (6.3.2) gives the time dependent equation for charge across the capacitor.

$$Q(t) = C \cdot V_{\max} \cdot \sin(\omega t) \tag{6.3.4}$$

Current is the first time derivative of charge given by Equation(6.3.5).

$$I = \frac{dQ}{dt} = \omega \cdot C \cdot V_{\max} \cdot \cos(\omega t) \tag{6.3.5}$$

Equation (6.3.6) is used to convert frequency in radians/sec, ω, to hertz, f.

$$\omega = 2\pi f \tag{6.3.6}$$

The maximum current will be drawn from the power supply when the cosine term in Equation (6.3.5) is equal to 1 as shown in Equation(6.3.7).

$$I_{\max} = 2\pi f \cdot C \cdot V_{\max} \tag{6.3.7}$$

Therefore the maximum frequency is given by Equation(6.3.8).

$$f = \frac{I_{\max}}{2\pi \cdot C \cdot V_{\max}} \tag{6.3.8}$$

The capacitance of the stacks is ~9 μF and the maximum current that can be sourced by the amplifier is 200mA. The maximum drive voltage for the EPCOS PZT stacks of 160V. Substituting these values in Equation(6.3.8) results in a maximum theoretical frequency of 22.1 Hz. This theoretical result does not match the experimental one exactly but there is variation in the capacitance between different stacks and the calculations also assume the manufacturers stated current limit is correct.

To experimentally validate the frequency roll off is directly attributed to the amplifier current limit; the drive voltage was reduced by 50 percent to $80V_{pp}$. This should result in a frequency limit 44.2 Hz, twice the limit using $160V_{pp}$. Figure 6.3.4 shows a comparison between the displacement results obtained using drive voltages of $80V_{pp}$ and $160V_{pp}$.

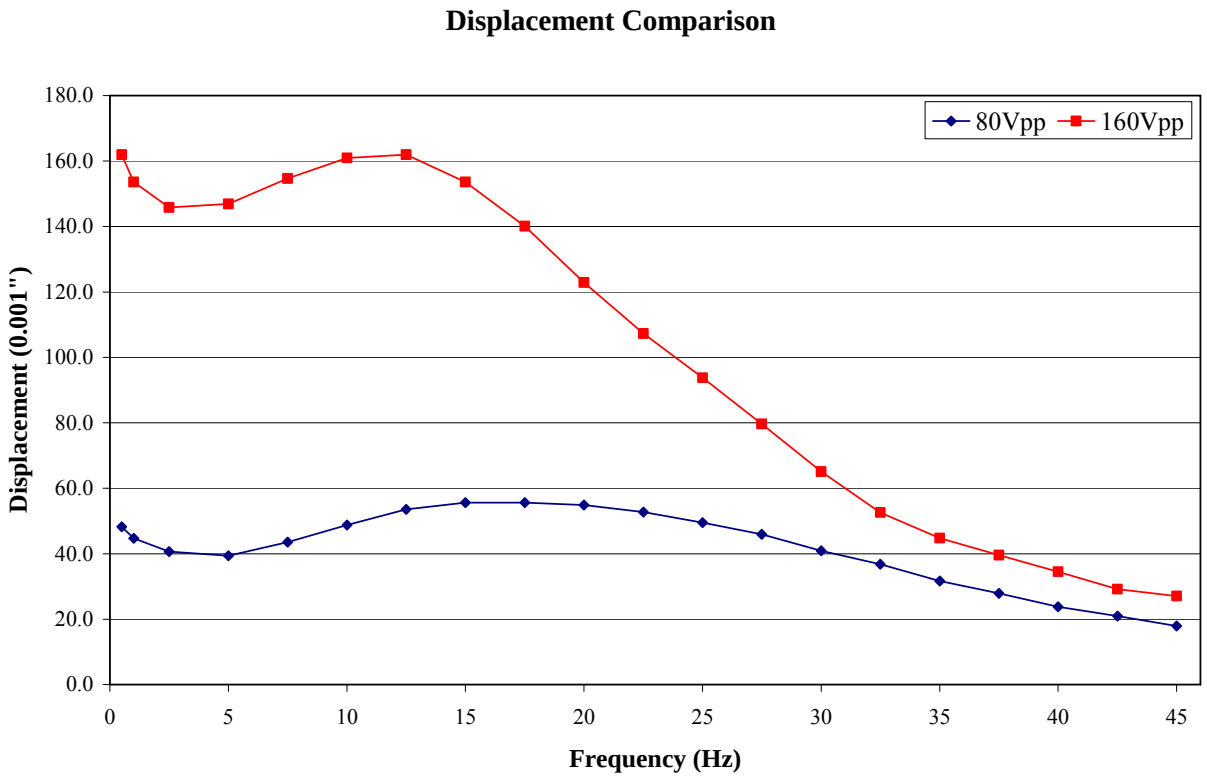

Figure 6.3.4: Displacement comparison between 80 V_{pp} and $160V_{pp}$ drive voltages

Reducing the drive voltage delayed the frequency roll off, but did not double the frequency as expected. Therefore some of the roll off can be attributed to dissipative losses in the fluid. Figure 6.3.5 shows the results of the $80V_{pp}$ tests with error bars depicting the 95 percent confidence interval.

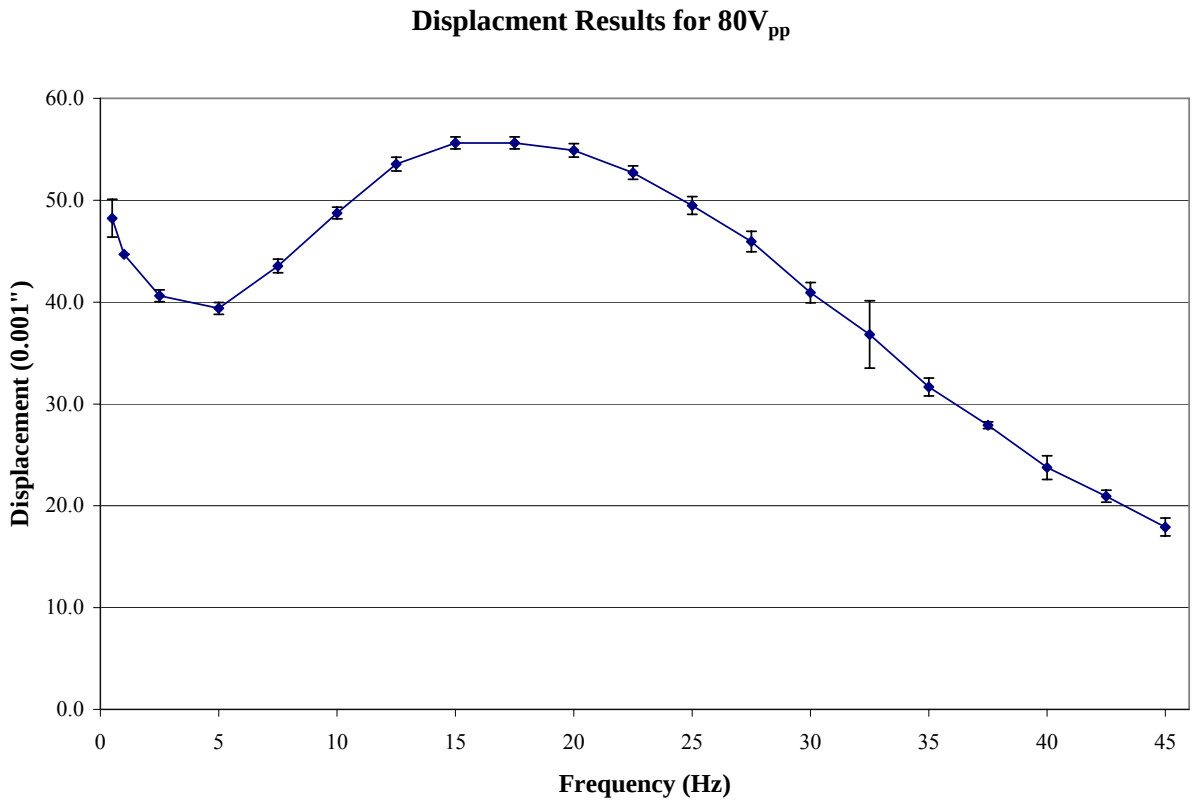

Figure 6.3.5: Displacement results for test using $80V_{pp}$ drive voltages with error bars

The results shown in the previous figure are the averaged results for three trials. The error bars were calculated using equation(6.3.1).

The small dip in performance from 2.5 – 7.5 Hz shown in the previous data sets may be attributed to a laminar to turbulent transition in the fluid. The peak fluid velocity in and

oscillatory flow, v_f, which occurs in the tubing can be calculated as a function of frequency, f, using Equation(6.3.9).

$$v_f = \frac{2 f \Delta l_s N_m A_p}{A_t} \tag{6.3.9}$$

Where Δl_s is the stack displacement, N_m is the mechanical amplification ratio, A_p is the area of the piston, A_t is the area of the tubing. Using the velocity, a Reynolds number, Re, can be calculated using Equation(6.3.10).

$$\mathrm{Re} = \frac{\rho v_f D_t}{\mu} \tag{6.3.10}$$

The density, ρ, for the fluid used is 757.77 kg/m^3 and the viscosity, μ, is 4.93 x 10^{-4} kg/(m-s). For operating frequencies of 2.5 and 7.5 Hz the Reynolds number are 2688 and 8065 respectively. For internal flow, the transition from laminar to turbulent occurs at a Reynolds number between 2100 and 4000, which corresponds to the Reynolds numbers calculated for the system for 2 and 5 Hz.

6.4 Force Testing

The displacement was characterized as a function of applied force. The force was applied to the system by hanging weights from the hydraulic actuator as mentioned in a previous section. The testing was conducted using a drive voltage of 160 V_{pp} at a frequency of 1 hertz. Figure 6.4.1 shows the results of the force testing.

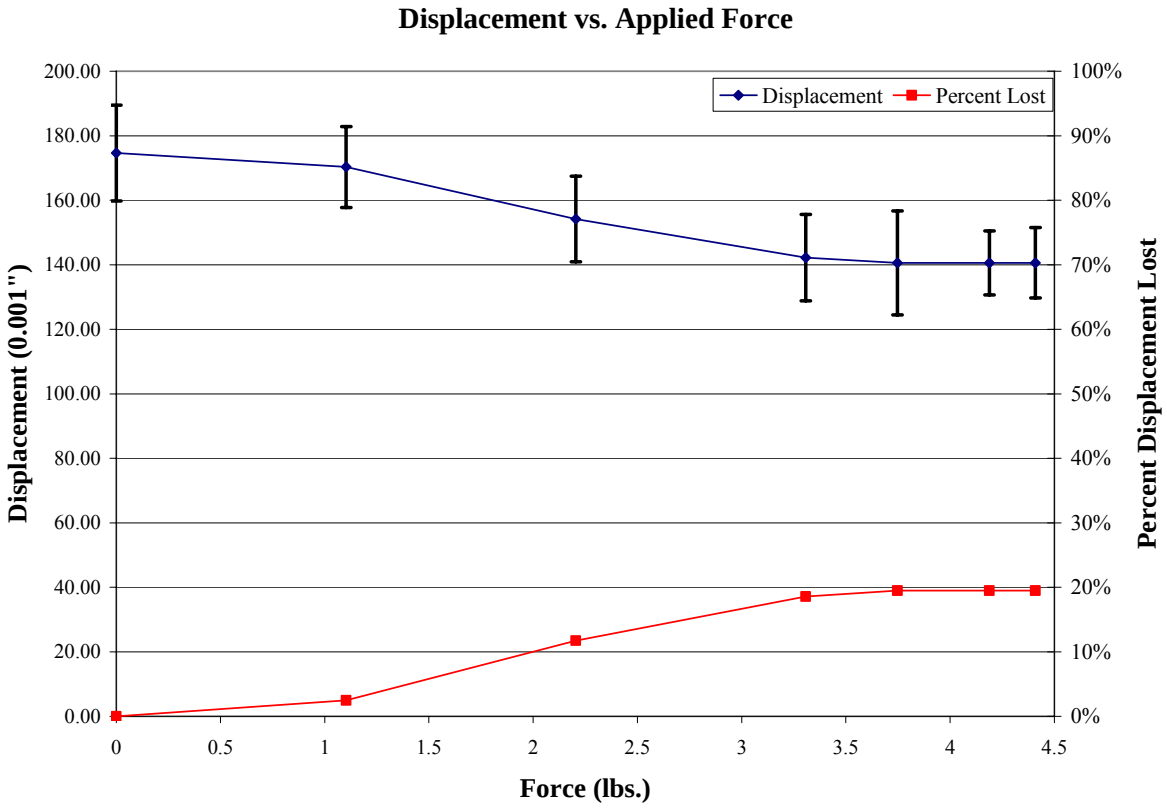

Figure 6.4.1: Results from force testing

Also shown in the previous figure is the percent displacement lost do to the applied force. The forces applied to the actuator were limited to less than 5 pounds due to the large forces that would be experienced by the piezoelectric stacks. Application of a 4.41 pound (2 kg) force to the actuator resulted in a 19.5% reduction in displacement output.

CHAPTER 7: CONCLUDING REMARKS

A proof of concept helicopter trailing edge flap actuator was designed and tested. The system amplified the motion of a piezo stack 52 times; the result was an experimentally measured free displacement of 4.369 mm (0.172 in), which is 70% of the theoretically calculated value of 6.24 mm (0.246 in). The testing results identified that the electrical amplifiers used to drive the piezoelectric stacks could not provide sufficient current to test the device throughout its entire operating range. The amplifiers limited higher frequency testing of the device. The stacks used would require 362mA in order to operate throughout the entire bandwidth of 0 – 40 Hz. Testing also identified there may be some dissipative-viscous effects in the fluid that may impede higher frequency operation of the device.

As the price of single crystal piezoelectric materials continue to decrease, it will become feasible to use them as replacements for PZT in actuation systems. This will further enhance the performance of the actuation systems. Table 7.1 was generated to compare performance between the EPCOS PZT stacks used in this investigation and single crystal PMN-PT stacks with 0.25mm layers of identical cross-section.

Table 7.1: Comparison of EPCOS PZT and Single Crystal PMN-PT Stacks

	EPCOS PZT	**Single Crystal PMN-32PT Stacks**
Material Properties		
Modulus, Y_3	30 GPa	14 GPa
Piezo Coefficent, d_{333}	750 pN/C	2250 pN/C
Relative Dielectric Constant, K_3	~1750	8000
Electrical Requirements		
Electric Field, E_3	2 MV/m	2 MV/m
Voltage, V_{max}	160 V	500 V
Current@40Hz, I_{max}	361.9 mA	589.1 mA
Stack Properties		
Cross Sectional Area, A_s	46.24 mm^2	46.24 mm^2
Length, l	90 mm	90 mm
Layer Thickness, t	80 μm	0.25 mm
Number of layers, n	~1000	358
Capacitance, C	9.00 μF(*)	4.69 μF
Stack Ouput		
Free Strain, ε_f	0.001333 (*)	0.004 (*)
Blocked Stress, σ_b	25 Mpa(*)	56 MPa
Free Displacment, Δ_{stack}	120 μm(*)	360 μm
Blocked Force, $F_{b,stack}$	1156.0 N	2589.4 N
Amplification Ratios		
Mechanical Amplification Ratio, N_m	5	5
Hydraulic Amplification Ratio, N_H	10.4	10.4
Total Amplification Ratio, N_t	52	52
System Output		
Calc. Free Displacement, Δ_{system}	6.24 mm	18.72 mm
Calc. Blocked Force, $F_{b,system}$	22.23 N	49.80 N

The values in the Table 7.1 can be calculated using Equations(7.1.1)-(7.1.8). The values marked with an asterisk, '*', are not calculated, but obtained from the manufacturer's datasheets. The capacitance of a piezoelectric stack can be calculated using Equation(7.1.1):

$$C = \frac{n K_3 \varepsilon_0 A_s}{t} \tag{7.1.1}$$

where ε_0 is the permittivity of free space, 8.85 x10^{-12} F/m. Using the linear constitutive relationships for piezoelectrics, the free strain produced by the stacks is given by Equation(7.1.2)

$$\varepsilon_f = d_{333} E_3 \tag{7.1.2}$$

Application of Equation(7.1.2) to the EPCOS PZT and PMN-32PT stacks, gives free strains of 1500 and 4500 microstrain respectively. Due the non-linear material behavior, the free strain will reach saturation levels of 1333 and 4000 microstrain respectively, which are used in the remaining calculations. The blocked stress can be estimated using Equation(7.1.3).

$$\sigma_b = Y_3 \varepsilon_f \tag{7.1.3}$$

The block stress for soft PZT, which is used in the EPCOS stacks, saturates around 25MPa and this saturation value is used for the remaining calculations. The stack free displacement and blocked force can be calculated using Equation(7.1.4) and (7.1.5).

$$\Delta_{stack} = l \varepsilon_f \tag{7.1.4}$$

$$F_{b,stack} = A_s \, \sigma_b \tag{7.1.5}$$

The total amplification ratio is given by Equation(7.1.6).

$$N_t = N_m N_H \tag{7.1.6}$$

The displacement and blocked force developed by the system is given by Equation(7.1.7) and (7.1.8).

$$\Delta_{system} = N_t \, \Delta_{stack} \tag{7.1.7}$$

$$F_{b,system} = \frac{F_{b,stack}}{N_t} \tag{7.1.8}$$

The substitution of single crystals for the PZT will provide and additional 200 percent increase in free displacement and a 124 percent increase in blocked force. This represents a substantial improvement to the current design, achieved only by substituting the piezoelectric material. Another benefit to the use of PMN-PT single crystals is they exhibit far less hysteresis than PZT, which will reduce the heat generated by the stacks when driven at higher frequencies. Materials research working on the development of PMN-PT has shown that it may be possible to achieve strain levels of 6000 microstrain from these materials. This would further increase the performance of the devices utilizing these materials.

The work performed in this study was part of a phase one program. As a result of success of the work performed under phase one, a second phase contract has been awarded. The second phase will focus on developing a flight-worthy actuator that will fit in a main rotor blade.

This actuator will be capable of meeting the performance requirements for vibration suppression listed earlier. Testing will focus on in-blade endurance testing, to determine device endurance. Also the device will be mounted in a blade section and tested in a spin chamber to examine the effects of the centrifugal load on device performance.

REFERENCES

176-1987, A. I. S. **IEEE Standard on Piezoelectricity**. **ANSI/IEEE Std 176-1987**.

Ben-Zeev, O. and I. Chopra (1996). "Advances in the development of an intelligent helicopter rotor employing smart trailing-edge flaps." Smart Materials and Structures **5**(1): 11-25.

Chopra, I. and J. Shen (2004). "Swashplateless Helicopter Rotor with Trailing Edge Flaps." Journal of Aircraft **41**(2): 208-214.

Jaffe, B., W. R. Cook, et al. (1971). Piezoelectric ceramics. London, New York, Academic Press.

Lynch, C. S. (1996). "The effect of uniaxial stress on the electro-mechanical response of 8/65/35 PLZT." Acta Materialia **44**(10): 4137.

Physik Instrumente. (1996). Retrieved September 14, 2005, from www.physikinstrumente.de.

Piezo Systems, I. (2002). History of Piezoelectricity Retrieved September 14, 2005, from www.piezo.com.

Prechtl, E. F. (1994). Development of a Piezoelectric Servo-Flap Actuator for Helicopter Control, Massachusetts Instituite of Technology. **Master's Degree**.

Prechtl, E. F. and S. R. Hall (1999). "Design of a high efficiency, large stroke, electromechanical actuator." Smart Materials and Structures(8): 13-30.

Spangler, R. L. (1989). Piezoelectric Actuators for Helicopter Rotor Control, Massachusetts Institute of Technology. **Master's Thesis**.

Straub, F. and B. Derham. (2000). "Smart Materials and Structures Demonstrations: Smart Rotors." Retrieved September 15, 2005, from http://www.darpa.mil/dso/thrust/matdev/chap/briefings/timchap2000day1/straub_derham.pdf.

Straub, F. K., D. K. Kennedy, et al. (2004). "Development and Whirl Tower Test of the SMART Active Flap Rotor." Smart structures and materials 2004: Industrial and commercial applications of smart structures technologies **5388**: 202-212.

Straub, F. K., H. T. Ngo, et al. (2001). "Development of a piezoelectric actuator for trailing edge flap control of full scale rotor blades." Smart Materials and Structures(10): 25-34.

Trainer, M. (2003). "Kelvin and Piezoelectricity." European Journal of Physics **24**(5): 535-542.